POLITECNICO DI TORINO
Repository ISTITUZIONALE

Experimental investigation and dataset release of a taut-leg mooring system for a semi-submersible floating offshore wind turbine

Original
Experimental investigation and dataset release of a taut-leg mooring system for a semi-submersible floating offshore wind turbine / Niosi, F., Dell'Edera, O., Glorioso, M., Paduano, B., Giorgi, G., Schreier, S.. - In: OCEAN ENGINEERING. - ISSN 0029-8018. - 328:(2025). [10.1016/j.oceaneng.2025.121067]

Availability:
This version is available at: 11583/2999988 since: 2025-05-09T06:59:46Z

Publisher:
Elsevier

Published
DOI:10.1016/j.oceaneng.2025.121067

Terms of use:

This article is made available under terms and conditions as specified in the corresponding bibliographic description in the repository

Publisher copyright

(Article begins on next page)

19 November 2026

An update to this article is included at the end

Ocean Engineering 328 (2025) 121067

Contents lists available at ScienceDirect

Ocean Engineering

journal homepage: www.elsevier.com/locate/oceaneng

Research paper

Experimental investigation and dataset release of a taut-leg mooring system for a semi-submersible floating offshore wind turbine

Francesco Niosi [a,1,*], Oronzo Dell'edera [a], Mattia Glorioso [a], Bruno Paduano [a], Giuseppe Giorgi [a], Sebastian Schreier [b]

[a] Marine Offshore Renewable Energy Lab (MOREnergy Lab), Department of Mechanical and Aerospace Engineering (DIMEAS), Politecnico di Torino, Via Duca Degli Abbruzzi, 24, Turin, 10129, Italy

[b] Delft University of Technology, Fac. Mechanical Engineering, Dept. Maritime Transport Technology, Ship Hydromechanics, Mekelweg 2, Delft, 2628 CD, the Netherlands

ARTICLE INFO

Keywords:
Floating offshore wind turbine
Taut mooring system
Mooring stiffness
Experimental campaign
Environmental contours
Irregular
Regular
Multisine waves

ABSTRACT

In the offshore wind energy field, reducing energy costs involves optimizing and analyzing each system component. A key component influenced by the installation site is the mooring system, which can be designed using various concepts. This study focuses on examining a taut-leg mooring system and its impact on the overall system behavior. Due to a lack of experimental data on taut-leg mooring systems for Floating Offshore Wind Turbines (FOWTs) in the existing literature, our work aims to provide the scientific community with an extensive experimental dataset to validate various numerical models and support the design process of a taut-leg mooring system for a selected installation site.

The full-scale mooring system was designed, scaled down, and evaluated through experiments at a 1:96 scale using a mooring configuration realized with springs. Springs offer a constant axial stiffness, reflecting the ideal structural behavior. Our paper highlights significant observations for this configuration, even under off-design conditions with modified pre-tension levels. Regular and irregular waves were tested to establish a baseline hydrodynamic response, assess the wind turbine's impact on the floater, and evaluate operating conditions. An environmental contour (EC) was defined to analyze the system's behavior in ultimate and accidental limit states. System identification (ID) waves streamlined the characterization process by reducing the number of required waves. Additionally, free decay tests were performed to assess the system's dynamic characteristics at resonance. The analysis of experimental data reveals that pre-tension variations minimally influence the dynamics of the floating structure. Results showed that the tested mooring system exhibits stability during power production and withstands ultimate and accidental limit states.

1. Introduction

The global challenge of climate change has prompted a relentless pursuit of sustainable energy solutions to reduce greenhouse gas emissions and transition towards a greener future. Within the global and European panorama of combating climate change and, consequently, of the production of green energy, Italy is actively participating in the European effort to achieve the zero emissions goal outlined in the Green Deal (The European Commission, 2023). In addition to the widespread decarbonization efforts in sectors like construction, industry, transportation, and agriculture, it's important to remember that smaller off-grid entities not connected to the national electrical grid also need to be included in the transition to a green economy.

Non-interconnected minor islands stand as unique entities with distinct geographical and energy characteristics. As part of the European Commission's efforts, the Clean Energy Secretariat for EU islands has set the stage for energy transition pathways through the Clean Energy Transition Agenda (CETA) instrument (Secretariat, 2023). Among these islands, Lampedusa, situated south of Sicily in the Mediterranean Sea, holds a special significance. Unlike mainland regions, it is not connected to the national electricity grid and solely relies on locally produced electricity derived from fossil fuels. As part of the "Isole Verdi" (PNRR, n.d.) project under the "Piano Nazionale di Ripresa e Resilienza," the urgency to decarbonize Lampedusa's energy supply has led to a pioneering initiative: the installation of a Floating Offshore Wind Turbine (FOWT).

* Corresponding author.
E-mail address: francesco.niosi@polito.it (F. Niosi).
[1] https://www.linkedin.com/profile/view?id=francesconiosi

https://doi.org/10.1016/j.oceaneng.2025.121067
Received 26 July 2024; Received in revised form 31 January 2025; Accepted 22 March 2025
Available online 31 March 2025
0029-8018/© 2025 The Authors. Published by Elsevier Ltd. This is an open access article under the CC BY license (http://creativecommons.org/licenses/by/4.0/).

To effectively design a FOWT and its mooring system, several factors have to be considered. Different mooring options have been explored, and the taut-leg mooring system emerged as the most promising for the Lampedusa installation site due to several advantages. Firstly, it is cost-effective compared to traditional catenary mooring systems (Bach-Gansmo et al., 2020). Secondly, a taut-leg system has shorter mooring lines and requires less seafloor space than a catenary mooring system. Moreover, the taut-leg system exhibits significantly higher linear stiffness compared to the catenary system. This offers several benefits, including improved control of offsets under average loads and reduced overall tension in the mooring lines. Additionally, the taut-leg system facilitates better load distribution among neighboring mooring lines. However, one drawback of this system is that the mooring lines must possess sufficient elasticity to absorb the floater's motions without becoming overloaded. For this reason, it is crucial to choose the right material so that the mooring lines have sufficient elasticity to absorb the motions of the floating body (Sørum et al., 2023).

Despite the relevance of the taut-leg mooring system for FOWTs, all the publicly available experimental datasets are related to catenary mooring systems. In (Stewart and Muskulus, 2016), a list of the main experimental campaigns published on offshore wind up to 2016 is reported. All the experimental campaigns reported in this work have a scale factor ranging from 22.5 to 105 and include various types of substructures and methodologies for reproducing the aerodynamic forces developed by the wind turbine. In fact, in Utsunomiya et al. (2009), a 2 MW turbine with a spar-type structure moored using catenary mooring was studied. The experimental campaign was conducted using both regular and irregular waves. The same type of substructure, the spar buoy, was also tested in Myhr et al. (2011) and (Myhr and Nygaard, 2015) with a tension leg mooring system and without wind-induced loads. On the other hand, in Roddier et al. (2010); Jonkman (2010); Azcona et al. (2014), semi-submersible substructures with catenary mooring systems are experimentally analyzed. In (Martin, 2011), catenary moorings are tested for spar, semi-submersible, and tension leg platform substructures, where wind loads are scaled to realistically simulate the turbine rotor. In more recent studies like (Lopez-Olocco et al., 2023), an experimental campaign was conducted on spar buoy platforms with a shared mooring catenary configuration. In (Hallak et al., 2022), a mooring system with constant stiffness and horizontally oriented mooring lines is tested, providing the substructure with predefined surge stiffness. The work presented in Robertson et al. (2020) uses the same substructure as the one used in this paper, employing a spring mooring system to reproduce the linear response of the system with the originally tested catenary mooring in Robertson et al. (2017). The same substructure was tested in a very recent study (Tagliafierro et al., 2023) using a mooring system consisting of springs, in which the hydrodynamic forces acting on the substructure were validated through DualSPHysics simulation tool (Martínez-Estévez et al., 2023).

The literature review, summarized above, highlights a substantial lack of comprehensive experimental data concerning taut-leg mooring systems. Therefore, the aim of our research activity was to characterize the 5MW NREL Wind turbine with the DeepCWind substructure utilizing an innovative taut-leg system that had been refined through genetic algorithms.

The campaign aimed to characterize the system's response under various conditions, including operational, extreme, and off-design scenarios. To define the hydrodynamic response of the moored substructure, tests were conducted in regular waves with varying periods and steepness. These tests aimed to provide a cost-effective dataset for easy validation with high-fidelity numerical models like CFD (Computational Fluid Dynamics). To efficiently characterize the dynamic response of the system across the entire range of frequencies of interest, tests with variable amplitude multisine waves were performed. By varying the amplitude of individual multisine waves, it was possible to define the nonlinearities of the moored system. These two sets of waves were tested for modeling and dynamic characterization purposes. On the other hand, tests in irregular waves were intended to characterize the response of the system installed off the coast of Lampedusa under real operational conditions during which a thrust force correlated to the wind speed is applied at the nacelle. These tests were designed following a thorough analysis of the meteorological and marine conditions at the site detailed in Section 4. In these tests, wind force was applied to the rotor statically using an actuator line connected to the tower through a fairlead positioned at the rotor's height. Irregular waves not only allowed the determination of the system's dynamics under operational conditions but also assessed the turbine's energy production. Finally, for the purpose of structural integrity verification under adverse weather and marine conditions, Ultimate Limit State (ULS) and Accidental Limit State (ALS) tests were conducted. The extreme event associated with these tests was defined using the methodology detailed in DNV (DNVGL-RP-C205, 2017). Under ALS conditions, various damage scenarios were simulated, including the disconnection of the bow mooring line, one of the two stern mooring lines, and the simulation of actuator failures responsible for pitch control of the blades. The insights gained from these tests provided critical guidance for designing taut-leg mooring systems and underscored the importance of considering pre-tensioning levels in a mooring system composed by lines with constant stiffness. This dataset would not only support the design of taut-leg mooring systems for FOWTs but also contribute to the broader field of floating offshore wind energy. To maximize the impact of this research and support the broader scientific community, the experimental data is available for download at the following link or can be found by reference Niosi et al. (2023b). The detailed list of the tests performed can be found in Appendix A. However, it is essential to acknowledge the limitations of the study, particularly the small model scale of 1:96 and the assumption of constant thrust during the tests. Working at this scale introduces potential challenges due to scale effects, as certain hydrodynamic and structural responses may not directly translate from model scale to full scale. Nonetheless, scaling down a taut leg mooring system is less affected by these scaling issues than other mooring configurations, such as catenary moorings, because the primary forces governing taut mooring systems are largely based on linear stiffness and tension properties. Studies such as Robertson and Jonkman (2011) suggest that tension-dominant mooring systems exhibit more consistent behavior under scaled testing conditions, as their response relies primarily on mass and stiffness, which are less sensitive to scale-induced variations.

While viscous damping could be influenced by the reduced scale, existing studies indicate that its effect is generally minor for structures with low-amplitude motions, such as those with taut moorings (Thiagarajan and Troesch, 1994). Furthermore, in Kimball et al. (2005) emphasize that, while precise hydrodynamic scaling can be challenging to achieve, the mooring stiffness dominates the response of taut mooring systems, thus reducing the criticality of exact hydrodynamic scaling. To address these considerations, we used calibration procedures for instrumentation and conducted sensitivity and repeatability analyses to ensure data reliability. These procedures showed that potential measurement errors had a limited impact on the final results. We acknowledge, however, that while these methods improve experimental accuracy, they do not fully eliminate scale effects, and we have incorporated relevant literature to contextualize these limitations.

2. Floater design overview

This study focuses on investigating the mooring system configuration for a semi-submersible substructure, specifically the DeepCWind model from the OC5 project (Robertson et al., 2015). Unlike the OC5 project, which utilized a 1:50 scale and the deep MARIN basin, this research aims to assess the mooring system for installing a turbine in the Mediterranean Sea, particularly in Lampedusa, Sicily. The research employs a 1:96 scale model due to the constraints of the wave tank used for the experiment.

The DeepCWind scaled model consists of four columns: three outer columns and one inner column supporting the wind turbine. The model is constructed using PVC pipes, with sizes of 125 mm and 250 mm for the high columns and heave plates, respectively. The middle column is built using a 63 mm pipe. The heave plates attached to the outer columns serve as connection points for the mooring lines. Interconnections between the outer columns and the inner column are facilitated by steel rods at the top and bottom, with additional shear resistance provided by three inclined rods towards the inner column. The wind turbine is simulated using a 2 m vertical carbon fiber rod installed in the central column, with a nose cone connecting the tower to the actuator line, which applies a constant force to simulate the thrust generated by the turbine when activated by the wind. In the context of FOWTs, the primary environmental loads consist of hydrodynamic and aerodynamic forces. Achieving accurate motion and dynamic responses necessitates simultaneous simulation of these loads. However, satisfying both Reynolds and Froude scaling laws simultaneously at the model scale is impractical (Chen et al., 2022). Given that hydrodynamic loads contribute significantly to the environmental load and Froude scaling is more readily met at model scale, experiments are typically conducted under Froude scaling law. Under Froude scaling, hydrodynamic loads can be simulated comprehensively and accurately, albeit at the cost of reduced aerodynamic loads faithfull representation due to lower Reynolds numbers. Consequently, major aerodynamic performance characteristics of the rotor, such as thrust coefficient (CT), power coefficient (CP), and tip speed ratio (TSR), are considered. To establish equivalence in aerodynamic performance, the scaled-down model's CT, CP, and TSR must match those of the full-scale prototype across various wind speeds. CT, CP, and TSR are closely related to aerodynamic thrust, torque, and rotor speed, respectively. Aerodynamic thrust primarily affects global motion responses, torque influences rotor control strategies, and rotor speed impacts gyroscopic moments and frequency multiplication forces. During rotor model scaling, achieving equivalence in aerodynamic thrust is prioritized over aerodynamic torque and rotor speed. To realize the equivalence of aerodynamic loads under the Froude scaling law, the most common approach is to simulate the major components of aerodynamic loads, while neglecting the minor components. Since this study aims to characterize the global motion responses primarily influenced by hydrodynamics, mooring, and turbine thrust, we adopted an approach using an actuator line to replicate only the thrust effect. In reality, forces slightly vary during the test as the substructure motions affect the actuator line held in tension by a wind winch. This approach substantially simplifies the experimental setup. Further details of the model construction and the characteristics of the constant-tension winch can be found in Metsch (2023). The geometric characteristics of the scaled model are illustrated in Fig. 1, while Table 1 presents the inertial properties of the scaled model against the prototype scaled characteristics. The target column refers to the scaled value of the full-scale prototype detailed in Robertson et al. (2014). From the table, it can be seen that all errors

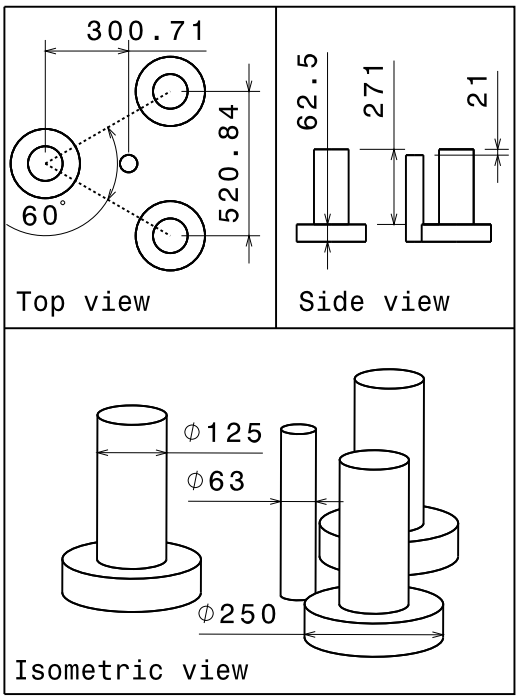


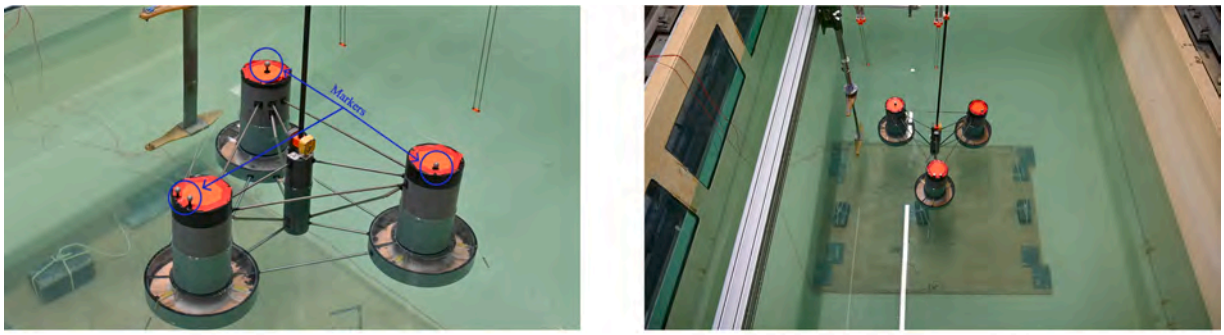
Fig. 1. Substructure dimensions in isometric, side, and top views (all dimensions in mm).

Table 1
Inertia properties of the model-scaled vs. prototype scaled value (target column).

Property	Measured	Target	Unit of measure	Relative error (%)
Mass	15.90 ± 0.01	15.77	kg	0.82 %
I_{xx}	1.772 ± 0.036	1.710	kg m^2	3.6 %
I_{yy}	1.788 ± 0.030	1.907	kg m^2	−6.7 %
I_{zz}	1.22 ± 0.03	1.379	kg m^2	10.9 %
CoG from bottom	128 ± 2	125	mm	2.4 %
Draft (Free-Floating)	208 ± 2	208	mm	< 0.1 %

are below 7 %, except for the one related to the yaw inertia moment I_{zz}. Since the experimental campaign will only include head sea tests, this error does not significantly affect all the measurements that will be taken during the tests.

The constructed scaled model is shown in Fig. 2. In the same figure, it is also possible to observe the wooden board used to attach the mooring system described in the following section.



(a) Model-scale FOWT (b) Mooring Experimental Mockup

Fig. 2. Mooring configurations sketch.

3. Mooring description

The mooring system of the floating turbine has been designed using a genetic algorithm aimed at minimizing the cost of the mooring system and the structural dynamics in both Maximum Operative Sea State (MOSS) and Ultimate Limit State (ULS) sea states which, for this case study, coincide respectively to the sea states IW_OP_05 (MOSS) and IW_EX_PR (ULS) described in Section 4. In this study, we focus on the optimization of a taut mooring system composed of three equally spaced lines. Although taut mooring systems are generally employed in deep waters, in this study, we adopt this configuration due to the constraints of the optimization workflow. The genetic algorithm used for the mooring system design is specifically formulated to handle taut mooring configurations, limiting the exploration of other mooring types. Nevertheless, this choice allows us to systematically investigate the performance, advantages, and limitations of taut mooring systems at intermediate water depths, a topic that remains underexplored in the existing literature. The optimization variables are: Anchor Radius, Rope Material, Rope Diameter, Line Length, and Chain Diameter. The five variables are free to vary between specific boundaries. The optimization workflow uses a Non-Sorted Genetic Algorithm-NSGA-II (Deb et al., 2002), which aims to minimize system cost and motion while adhering to specific physical constraints, detailed as follows:

- **Natural Periods Check:** To avoid resonance, the natural periods of the structure must satisfy the following conditions for surge, heave, and pitch modes:

$$T_{d,\text{Surge}} \approx T_{n,\text{Surge}} = 2\pi\sqrt{\frac{M + A_{11\infty}}{K_{11\text{moor}}}} > T_{\text{Surge, min}} \tag{1}$$

$$T_{d,\text{Heave}} \approx T_{n,\text{Heave}} = 2\pi\sqrt{\frac{M + A_{33\infty}}{K_{33\text{hydro}} + K_{33\text{moor}}}} > T_{\text{Heave, min}} \tag{2}$$

$$T_{d,\text{Pitch}} \approx T_{n,\text{Pitch}} = 2\pi\sqrt{\frac{I_{55} + A_{55\infty}}{K_{55\text{hydro}} + K_{55\text{moor}}}} > T_{\text{Pitch, min}} \tag{3}$$

  where:
  - $T_{d,\text{Surge}}$, $T_{d,\text{Heave}}$, and $T_{d,\text{Pitch}}$ are the resonance periods in the surge, heave, and pitch directions, respectively.
  - $T_{n,\text{Surge}}$, $T_{n,\text{Heave}}$, and $T_{n,\text{Pitch}}$ represent the natural periods in the surge, heave, and pitch directions.
  - M denotes the total mass of the structure.
  - I_{55} represents the pitch inertia of the structure.
  - $A_{11\infty}$, $A_{33\infty}$, and $A_{55\infty}$ are the added mass terms in surge, heave, and pitch at infinite frequency.
  - $K_{11\text{moor}}$ is the mooring stiffness in the surge direction.
  - $K_{33\text{hydro}}$ and $K_{33\text{moor}}$ are the hydrodynamic and mooring stiffness in the heave direction.
  - $K_{55\text{hydro}}$ and $K_{55\text{moor}}$ are the hydrodynamic and mooring stiffness in the pitch direction.
  - $T_{\text{Surge, min}}$, $T_{\text{Heave, min}}$, and $T_{\text{Pitch, min}}$ are the minimum allowable natural periods for surge, heave, and pitch as specified by regulatory standards.

  If any natural period does not satisfy these minimum conditions, the individual solution is penalized.
- **Slack Conditions Check:** For taut mooring configurations, it is essential to prevent the mooring lines from reaching slack conditions, maintaining a minimum line tension when the turbine is at its maximum offset. To ensure this, the tension in the line, T_{min}, must satisfy:

$$T_{\text{min}} \geq 0.05 \cdot T_{\text{m}} \tag{4}$$

  where:
  - T_{min} is the minimum allowable tension on the mooring line.
  - T_{m} represents the pretension level of the mooring lines.

  This threshold ensures a minimum tension of 5 % of the pretension level, adjustable to project requirements.
- **Static Limits Check:** After static simulations, including both aerodynamic and hydrodynamic loads, the maximum system responses in surge, heave, and pitch are derived. Regulatory standards require that these responses do not exceed predefined maximum values:

$$X_{\text{max}} < \text{Max Allowable Offset} \tag{5}$$

$$\Phi_{\text{max}} < \text{Max Allowable Pitch} \tag{6}$$

  where:
  - X_{max} is the maximum allowable offset in the surge direction.
  - Φ_{max} is the maximum allowable pitch angle.

  These limits are project-specific and can be customized based on turbine characteristics. Violations of these constraints result in penalization. In this case X_{max} and Φ_{max} were selected based on Vigara et al. (2019), with their respective values set to 30 m and 7°.
- **Safety Factor Check:** The mooring line maximum tension must be below the line Minimum Breaking Load (MBL). Since the simulation model used within the optimization algorithm is quasi-static, it can only estimate the maximum predicted tension in the mooring lines. Therefore, the safety factor equation has been simplified as follows:

$$1.5 \cdot T_{f\text{max}} < \text{MBL} \tag{7}$$

  where:
  - $T_{f\text{max}}$ is the maximum achievable tension on the mooring line.
  - MBL represents the Minimum Breaking Load of the mooring line.

  This formulation is a simplification of the design practice prescribed by DNV guidelines, which define separate safety factors for the static and dynamic components of mooring loads. However, once the mooring system is selected, a full time-domain analysis is conducted to verify that the system meets the required safety factors according to DNV standards, accounting for both static and dynamic contributions as well as mooring system redundancy. This ensures the reliability and safety of the mooring system under maximum loads.
- **Static Check:** During each static simulation, the output is monitored to ensure that the simulation remains stable and completes successfully. MATLAB tracks the simulation status in Orcaflex, verifying that the generated individual does not cause the simulation to fail, become unstable, or get stuck.

The quasi-static simulations in MOSS and ULS, which are used to evaluate the system dynamics, are constructed by applying loads from wind and waves. Wave loads are modeled using first-order spectral theory, while wind loads are applied as static forces, increased by a portion accounting for turbulence effects. Wind turbulence is considered in the determination of the aerodynamic load applied in the quasi-static model. A time-domain simulation is performed with the turbine fixed in place, using a turbulent wind field corresponding to the wind speed that generates the maximum thrust force. The turbulence intensity, which depends on the site conditions, influences the wind time history and affects peak thrust forces. From this simulation, a cumulative probability distribution (CDF) of thrust peaks is constructed using a Generalized Extreme Value (GEV) distribution and the Peak Over Threshold (POT) method (Veritas and Lloyd, 2017). The 99th percentile thrust force is then extracted and used as the input for the quasi-static model, ensuring that the effects of turbulence are incorporated into the aerodynamic loads considered for mooring system optimization. A similar approach is applied for the ULS condition, but with the rotor in a parked condition, representing the extreme operational scenario where the turbine is not actively generating power. The Pareto front analysis aids in identifying trade-offs where cost reductions may lead to increased motion. The Capex calculations rely on cost functions developed by the MORE research group (MORE, 2023), and static and dynamic simulations are conducted through the MATLAB-Orcaflex interface (Ghigo et al., 2022). The detailed description of the genetic algorithm is out of the scope of this paper and is

Table 2
Fairlead and anchor position for the full-scale and the model-scale.

	Full-scale			Model-scale		
	X (m)	Y (m)	Z (m)	X (m)	Y (m)	Z (m)
$Fairlead_1(F_1)$	20.4	35.4	−14.0	0.213	0.369	−0.146
$Anchor_1(A_1)$	36.6	65.1	−100.0	0.381	0.678	−1.042
$Fairlead_2(F_2)$	−40.9	0.0	−14.0	−0.426	0.000	−0.146
$Anchor_2(A_2)$	−75.0	0.0	−100.0	−0.781	0.000	−1.042
$Fairlead_3(F_3)$	20.4	−35.4	−14.0	0.213	−0.369	−0.146
$Anchor_3(A_3)$	36.6	−65.1	−100.0	0.381	−0.678	−1.042

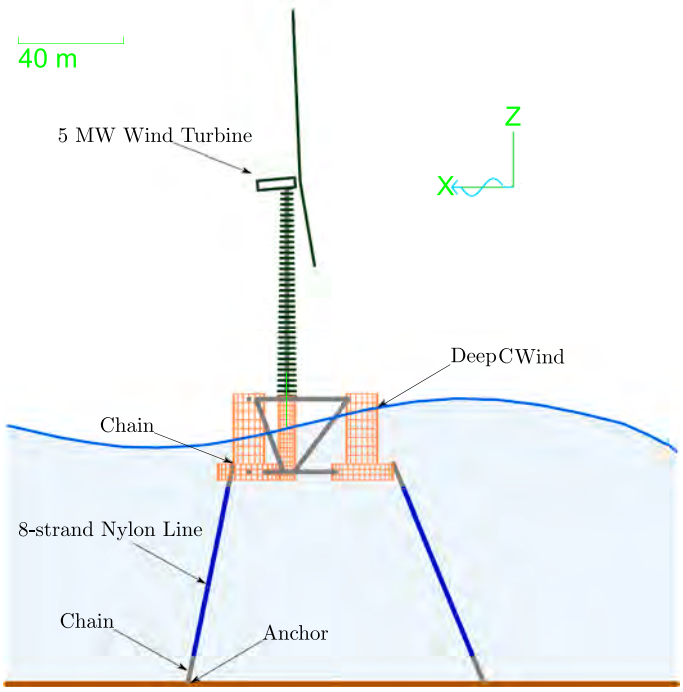


Fig. 3. Full-Scale Numerical Model Sketch.

yet to be published. Once the mooring system was selected from the Pareto front, scaling operations were carried out to prepare for the experimental tests. The full-scale model was designed with nylon mooring lines, assuming a constant stiffness value obtained from the OrcaFlex ® wizard. The axial stiffness was scaled down to determine the equivalent stiffness of the spring used in the experiments. To more accurately replicate full-scale conditions, a stiff polyester line was added after the spring in the model setup. This placement ensured that the polyester line did not affect the overall stiffness of the mooring system, as it is orders of magnitude stiffer than the spring. The main characteristics of the full-scale mooring system versus the model-scale parameters are presented in Tables 2 and 3; Fig. 3 shows the optimized mooring system used in the full-scale numerical model. The mooring system is designed for the installation site shown in Fig. 5, where the water depth is estimated to be 100 m. The optimization results have shown that both first and second-order hydrodynamic loads influence the mooring system design, especially in extreme conditions. In operative conditions, the most important effect on the mooring line is given by wind loads. For the optimization concerning this case study, nylon lines are the preferable solution for the mooring system due to their lower stiffness compared to polyester lines. Nylon lines allow resonance periods of the structure to be sufficiently distant from the sea spectra. However, for deeper water depths, this trend may change because the stiffness of the line decreases with its length. Nylon lines also can be a potential solution for other types of wind substructures, as they uniquely influence the resonance periods of low-frequency motions.

Table 3
Mooring description: full-scale vs. model-scale.

	Full-scale	UM	Scale factor (λ_s)	Model-scale	UM
Pre-Tension	1504	kN	3	1.7	N
Max Load (ULS/MOSS)	3200	kN	3	3.62	N
EA	17,622	kN	3	19.92	N
Nominal Diameter	386.4	mm	1	4.03	mm
Length of Nylon Rope	60.6	m	1	0.63	m
Axial Stiffness	290.9	kN/m	2	0.032	N/mm
Water Depth	100	m	1	1.04	m

It is important to acknowledge that a mooring system is subject to various forces, which can be categorized as follows:

- Mass-related forces: These forces arise from the inertial properties of the mooring line. The mass of the line contributes to its resistance to acceleration and deceleration, the added mass effect caused due to the surrounding fluid being accelerated by the mooring line, and the static weight of mooring lines, they affect the overall system dynamics.
- Drag-related forces: These forces result from the relative velocity between the mooring line and the surrounding fluid. The drag force is influenced by factors such as the flow velocity, the shape of the line, and the surface roughness, and it impacts the overall behavior of the mooring system.
- Stiffness-related forces: These forces can be further divided into two components:
  - Geometrical stiffness: This stiffness is associated with the geometry and configuration of the mooring line. It influences the response of the line to changes in position and shape, affecting the stability and motion of the system.
  - Axial stiffness: This stiffness relates to the axial properties of the mooring line, such as its material properties and cross-sectional area. It affects the resistance of the line to stretching and plays a role in the overall structural behavior of the mooring system.

It is indeed challenging to achieve a scaled version of each force component (Barltrop, 1998) of a mooring system. In the proposed experimental campaign, since we are dealing with a taut-leg mooring system, the axial stiffness is selected as the most influential force component in the system, and it is scaled accordingly. The choice made in this work is based on the understanding (Bach-Gansmo et al., 2020) that axial stiffness has a significant impact on the overall behavior of taut mooring systems. In other experiments, for instance, those analyzed in Niosi et al. (2023a), the mass properties of the mooring are scaled, not the stiffness properties. These decisions should be made based on the type of mooring being studied. In the context of this physical problem, adjusting the axial stiffness of the lines holds greater significance compared to scaling down the diameter of the line. The forces associated with line drag are expected to be minimal due to the absence of high dynamics experienced by the device and the mooring system, which does not exhibit characteristics of a catenary configuration where such effects could be more pronounced. To create the small-scale mooring model, a spring layout configuration (LCS) was adopted. Using springs with a constant stiffness allowed modeling the system under exact design conditions. This condition simplifies and speeds up numerical validation and can be implemented in real-life applications using spring mooring compensators (Seaflex, 2023). The scaling operations led to the mooring configuration shown in Fig. 4 and detailed in Table 5.

Table 4 presents a comparison of the diagonal components of the restoring mooring stiffness matrices for the full-scale prototype, the scaled model using a 1:96 Froude scaling, and the test model. The terms K_{11}, K_{22}, and K_{33} represent translational stiffness components with units of N/m, while K_{44}, K_{55}, and K_{66} denote rotational stiffness components in N m/rad.

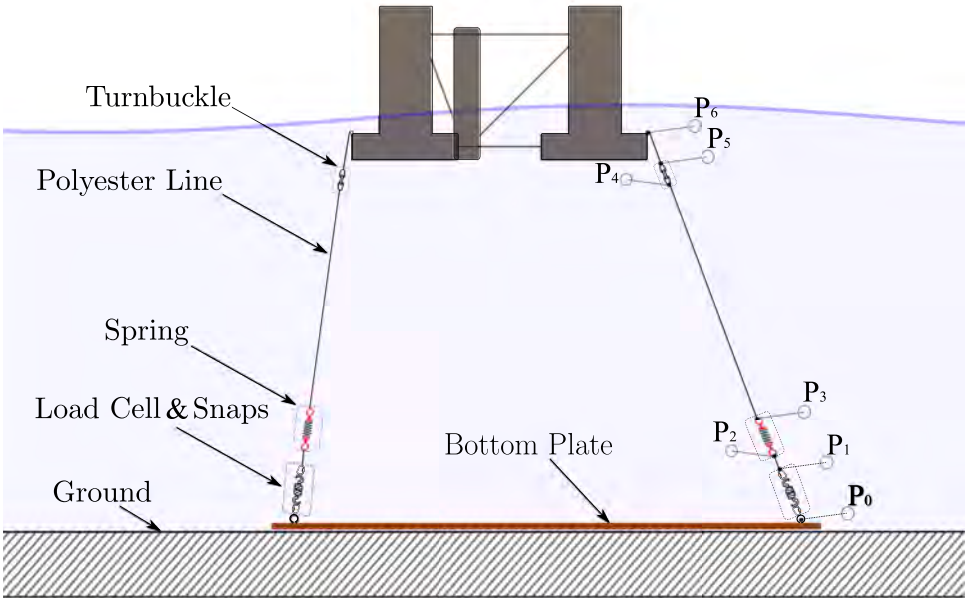


Fig. 4. Mooring layout configuration with Springs (LCS).

Table 4
Comparison of diagonal components of the restoring mooring stiffness matricx: full scale (prototype), scaled prototype values, and test model with percentage error.

Term	Unit	Full scale (Prototype)	Scaled (Prototype)	Model	Percentage error (%)
K_{11}	N/m	1.26×10^5	13.6	12.4	9.7
K_{22}	N/m	1.26×10^5	13.6	12.7	7.1
K_{33}	N/m	7.33×10^5	79.6	78.9	0.9
K_{44}	N m/rad	5.91×10^8	6.96	6.54	6.0
K_{55}	N m/rad	5.91×10^8	6.95	6.55	5.6
K_{66}	N m/rad	1.98×10^8	2.32	1.88	23.9

Table 5
Mooring characteristics for the springs configuration; each element is connected between two points (P), numbered as in Fig. 4. N.D. stands for Not Defined.

	Component	Unstreched length (mm)	Stiffness (N/m)	Supplier
P0-P1	Snaps + Load Cell	100.45	$K >> K_{spring}$	Futek
P1-P2	Polyester	45	$K >> K_{spring}$	N.D.
P2-P3	Spring	52	30.4	Lee Spring
P3-P4	Polyester	560	$K >> K_{spring}$	N.D.
P4-P5	Turnbuckle	44–66 (min-max)	$K >> K_{spring}$	N.D.
P5-P6	Polyester	45	$K >> K_{spring}$	N.D.

The 1:96 scale model consists of three mooring lines, each equipped with a spring in a water depth of 1 m. At the fairlead, a line tensioner (turnbuckle) is installed to ensure the appropriate pre-tension in the mooring lines. The turnbuckle ensures that the lines are adequately tightened to maintain the desired value of tension. At the anchor end of each mooring line, a load cell is employed to monitor and measure the forces exerted on the system. This load cell provides real-time data on the forces acting on the mooring lines, allowing for precise monitoring and adjustment as necessary. The length of the mooring lines, excluding the previously mentioned components, is made of polyester, chosen for its high stiffness and durability. The polyester, which is connected in series with the spring and has a very high stiffness, allows the mooring system to be characterized by considering only the linear stiffness of the spring.

Different pre-tension values were tested to investigate the behavior of the structure under off-design conditions. In fact, during the installation phase or when the mooring lines shorten over time (The SyR, 2018), the pre-tensions of taut lines may slightly differ from the design values. In Table 6, the different mooring configuration with varying pre-tension levels are reported. The design pre-tension value is indicate as LCS1 in Table 6. The pre-tension values refer to the average values of pre-tension, measured when the substructure is stationary and not subject to any aerodynamic or hydrodynamic loads. The pre-tension values are experimentally obtained by varying the turnbuckle extension.

Table 6
Mooring lines (ML) pre-tension levels.

Spring pre-tension values (N)			
	ML1	ML2	ML3
LCS1	**1.69**	**1.74**	**1.68**
LCS2	1.45	1.52	1.42
LCS3	1.18	1.26	1.17
LCS4	0.66	0.76	0.66
LCS5	2.49	2.26	2.23

For ease of numerical modeling of the presented mooring systems, it can be assumed that the lines are composed of a combination of a spring and a polyester line only in the LCS configuration. The drag coefficients of the lines can thus be ignored, which is a reasonable assumption given that the polyester line is very thin and the load cell and snap hooks are in the bottom of the tank, where velocities are quite low. Additionally, the turnbuckle can be omitted from the model since its weight and diameter do not significantly affect the overall dynamic behavior of the structure.

4. Metocean data analysis and experimental tests definition

This section presents the chosen tests, outlining the decision-making process for selecting the tests to be conducted. The site identified for the environmental analysis, presented in Fig. 5, was chosen as a case study for the “Isole Verdi” project, included in the “Piano Nazionale di Ripresa e Resilienza”.

The project involves the installation of a FOWT off the coast of Lampedusa Island, in order to integrate renewable energy into the island’s energy mix, which currently relies on fossil fuels only. Lampedusa Island is one of the many Italian island communities where electricity production occurs locally due to the lack of integration with the national electrical grid (Moscoloni et al., 2022). The current paper will not delve

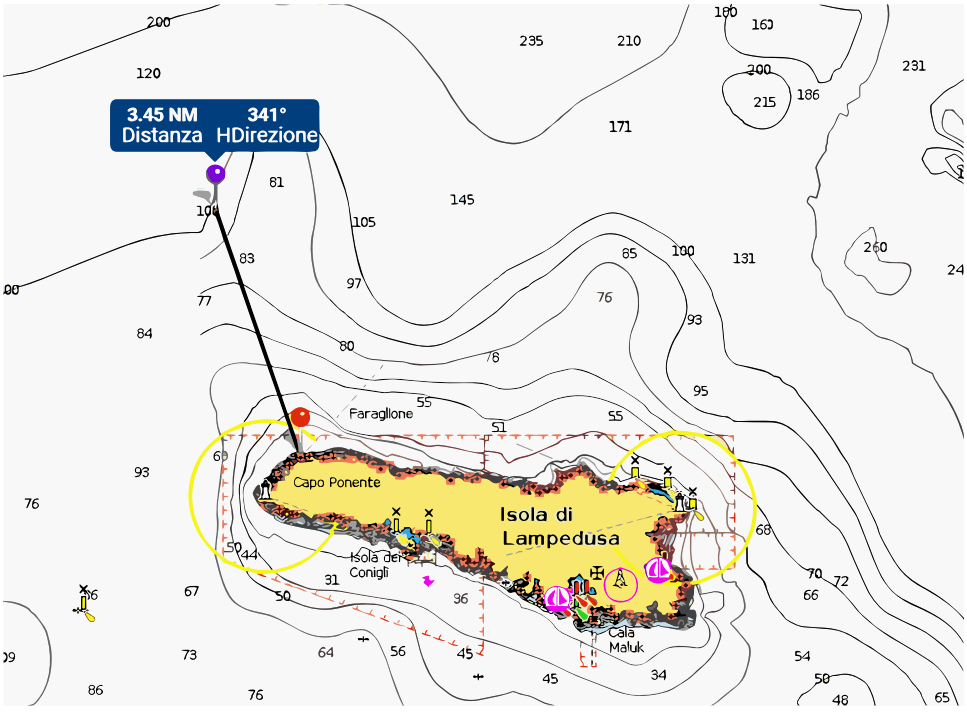


Fig. 5. Lampedusa Island, Mediterranean Sea: site location and marine traffic density layer.

Table 7
Installation site: main characteristics.

Country	Italy
Region	Sicily
Municipality	Lampedusa
Latitude	35.570 deg N
Longitude	12.498 deg E
Average Bathymetry	100 m
Average Wind Speed	7.4 m/s
Distance from Shore	3.45 NM
Distance from Cabin	5.79 NM
Marine Traffic Density	Low
Fishing Intensity	Low
Posidonia Oceanica	Not Present

Table 8
Test name convention.

Abbreviation	Meaning
ALS	Accidental Limit State
CA	Constant Amplitude
EX	Extreme
FD	Free Decay
IW	Irregular Wave
Moor	Test With Mooring
MS	MultiSine
ND	No Device
NW	No Wind
NoMoor	Test Without Mooring
OP	Operative Conditions
PR	Parked Rotor
RW	Regular Wave
s_i	Seed i_{th}
$St_{\max}$	Maximum Steepness

into the specific criteria (such as wind resource, sea state, water depth, etc.) that were used to select the site in question. In Table 7 are reported the main characteristics.

Once the site was defined, we proceeded to collect metocean data from the ERA5 database (Hersbach et al., 2020). This comprehensive dataset provides a wealth of meteorological and oceanographic information, including significant wave height (H_s), peak period (T_p), and wind speed (W_s). The dataset covers a period of 50 years and consists of measurements taken at three-hour samples. The waves selected in the experimental campaign are chosen to be representative of the statistical distribution found in the ERA5 dataset, compatible with the constraints in the facilities. Furthermore, additional tests were performed to assess the system dynamics which do not depend on the installation site.

Collectively, the experimental campaign encompassed a range of wave conditions and test scenarios, providing a comprehensive understanding of the system's response. Several types of tests were considered: regular waves, operative irregular waves, extreme irregular waves, system identification waves, and free decay tests. The convention used to define the names of the tests is listed in Table 8.

4.1. Regular waves

Regular waves are employed to establish a baseline response of the system under controlled conditions and without considering wind forces. Twelve regular waves are chosen, comprising 6 different frequencies of interest for one steepness, and 3 frequencies for each one of the other 2 steepness values. This selection aimed to explore the system's response and determine whether the system behaves as a linear mechanical system, thus the Response Amplitude Operator (RAO) of the device is constant irrespective of the wave height. Table 9 provides an overview of the tests conducted for this specific purpose.

4.2. Operative irregular waves

Irregular waves are considered fundamental tests during the experimental campaign as they aimed to capture the dynamic behavior of the system in ocean environments, under wind loading. With irregular waves, it is also possible to assess the turbine performances under realistic conditions. The irregular waves were defined using a JONSWAP Spectrum, with Γ equal to 3.3 as it is the most suitable for the Mediterranean Sea (Hasselmann et al., 1973). In operational conditions, we aim to test the system at a specific wind speed. To achieve this, we condition H_s and T_p on W_s to evaluate the most probable sea state values for a

Table 9
Regular waves: full-scale waves vs. model-scale values.

Wave name	Full-scale		Model-scale		
	H (m)	T (s)	H (mm)	T (s)	$Steepness(H/\lambda_w)$
RW_NW_OP_01	1.12	6.0	11.7	0.61	1/30
RW_NW_OP_02	1.53	7.0	15.9	0.71	1/30
RW_NW_OP_03	2.00	8.0	20.8	0.82	1/30
RW_NW_OP_04	2.53	9.0	26.3	0.92	1/30
RW_NW_OP_05	3.12	10	32.5	1.02	1/30
RW_NW_OP_06	4.49	12	46.8	1.22	1/30
RW_NW_OP_07	1.68	6.0	17.6	0.61	1/25
RW_NW_OP_08	3.00	8.0	31.2	0.82	1/25
RW_NW_OP_09	6.74	12	70.2	1.22	1/25
RW_NW_OP_10	2.81	6.0	29.3	0.61	1/20
RW_NW_OP_11	4.99	8.0	52.0	0.82	1/20
RW_NW_OP_12	11.2	12	117	1.22	1/20

Table 10
Operative irregular waves.

Wave name	Full-scale			Model-scale	
	H_s (m)	T_p (s)	W_s (m/s)	H_s (mm)	T_p (s)
IW_OP_01	1.29	6.09	3.0	13.4	0.62
IW_OP_02	1.37	6.19	5.0	14.3	0.63
IW_OP_03	1.50	6.36	7.0	15.6	0.65
IW_OP_04	1.67	6.58	9.0	17.4	0.67
IW_OP_05	1.91	6.86	11	19.9	0.70
IW_OP_05_s02	1.91	6.86	11	19.9	0.70
IW_OP_05_s03	1.91	6.86	11	19.9	0.70
IW_OP_05_s04	1.91	6.86	11	19.9	0.70
IW_OP_05_s05	1.91	6.86	11	19.9	0.70
IW_OP_06	2.20	7.19	13	22.9	0.73
IW_OP_07	2.56	7.57	15	26.7	0.77
IW_OP_08	3.00	8.01	17	31.3	0.82
IW_OP_09	3.52	8.50	19	36.7	0.87
IW_OP_10	4.13	9.04	21	43.0	0.92
IW_OP_11	4.83	9.62	23	50.3	0.98
IW_OP_12	5.62	10.2	25	58.5	1.05

given W_s. Thus, in this case, W_s serves as the independent variable. The JPDF of $H_s|W_s$ has been evaluated to determine the most likely H_s at a given W_s. To describe H_s a 3-parameter Weibull distribution is chosen. The location parameter of the distribution is fixed, while the scale and shape parameters vary based on the value of W_s:

$$f_{H_s|W_s}(x|w) = \begin{cases} \frac{k(w)}{\lambda(w)}\left(\frac{x-\gamma}{\lambda(w)}\right)^{k(w)-1} e^{-((x-\gamma)/\lambda(w))^{k(w)}}, & x \geq 0, \\ 0, & x < 0. \end{cases} \tag{8}$$

$$\lambda(w) = e_1 + e_2 w^{e_3} \tag{9}$$

$$\kappa(w) = f_1 + f_2 w^{f_3} \tag{10}$$

where γ is the location, λ is the scale, and κ is the shape parameter of the Weibull distribution. Subsequently, the most likely T_p was evaluated considering the JPDF of $T_p|H_s$. To describe T_p a lognormal distribution is chosen:

$$f_{T_p|H_s}(t|x) = \frac{1}{t\sigma(x)\sqrt{2\pi}} \exp\left(-\frac{(\ln(t)-\mu(x))^2}{2(\sigma(x))^2}\right) \tag{11}$$

$$\mu(x) = a_0 + a_1 x^{a_2} \tag{12}$$

$$\sigma(x) = b_0 + b_1^{-xb_2} \tag{13}$$

where μ is the mean, σ is the standard deviation of the natural logarithm of T_p and their functions are reported by Det Norske Veritas (DNV) in DNVGL-RP-C205 (2017). Table 10 illustrates the irregular wave conditions determined using this procedure. The irregular operational wave that resulted in the maximum thrust from the wind turbine (*IW_OP_05*) is generated using five different seeds.

4.3. Extreme irregular waves

For the analysis of extreme conditions, the Environmental Contour (EC) of the chosen site is evaluated. The construction of the EC follows the prescribed procedure outlined in the DNV standard (DNVGL-RP-C205, 2017). Unlike the operational case, W_S and T_p have been conditioned on H_s, which in this case is therefore the independent variable. The CDF of H_s has been described via a 3-parameter Weibull distribution:

$$F_{H_s}(x) = 1 - e^{-(\frac{x-\gamma}{\lambda})^{\kappa}} \tag{14}$$

T_p is described using a lognormal distribution conditioned on Hs:

$$F_{T_p|H_s}(t|x) = \frac{1}{2}\left(1 + erf\left(\frac{ln(t)-\mu(x)}{\sqrt{2}\sigma(x)}\right)\right) \tag{15}$$

W_s is described using a 2 parameter Weibull distribution conditioned on Hs:

$$F_{W_s|H_s}(w|x) = 1 - e^{-(\frac{w}{\lambda(x)})^{\kappa(x)}} \tag{16}$$

where λ is the scale and κ is the shape of the Weibull distribution. As for T_p the parameters of the CDF of W_s are described in function of H_s (DNVGL-RP-C205, 2017):

$$\kappa(x) = c_0 + c_1 x^{c_2} \tag{17}$$

$$\lambda(x) = d_0 + d_1 H_s^{d_2} \tag{18}$$

The value of the parameters based on the dataset are reported in Table 17. The EC was developed considering the probability associated with a return period of 100 years:

$$P_{100} = \left(\frac{1}{100 \cdot 365 \cdot \frac{24}{3}}\right) \tag{19}$$

where $365 \cdot \frac{24}{3}$ (three-hour samples) represent the number of event per year. The value of β, the radius of the sphere in Gaussian space, was determined by calculating the ICDF of the standard Gaussian function (with $\mu = 0$ and $\sigma = 1$) for the identified probability.

$$\beta = \Phi^{-1}(P_{100}) \tag{20}$$

$$u_1 = \beta \cos\theta \tag{21}$$

$$u_2 = \beta \sin\theta \cos\phi \tag{22}$$

$$u_3 = \beta \sin\theta \sin\phi \tag{23}$$

$$\theta[0, 2\pi] \qquad \phi[0, \pi] \tag{24}$$

The Gaussian space was transformed using the inverse of the CDFs identified previously:

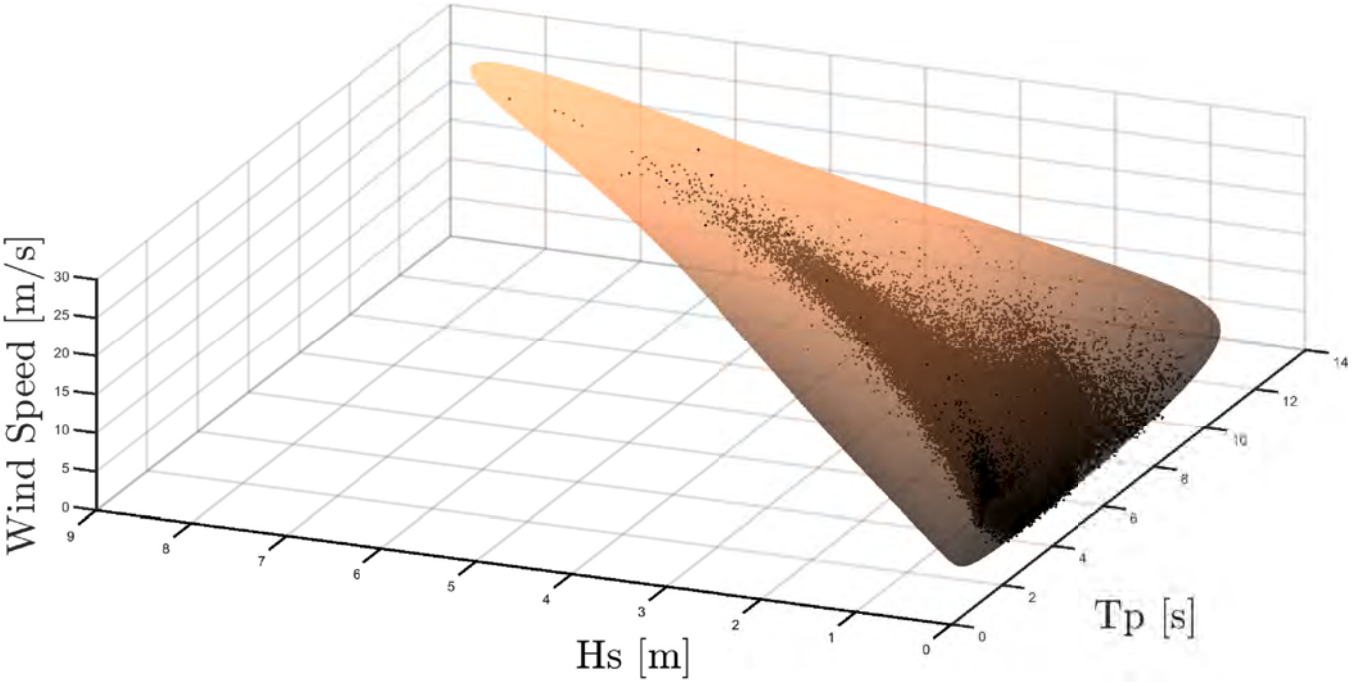
$$H_s = F_{H_s}^{-1}(\phi(u_1)) \tag{25}$$

$$T_p = F_{T_p|H_s}^{-1}(\phi(u_2)) \tag{26}$$

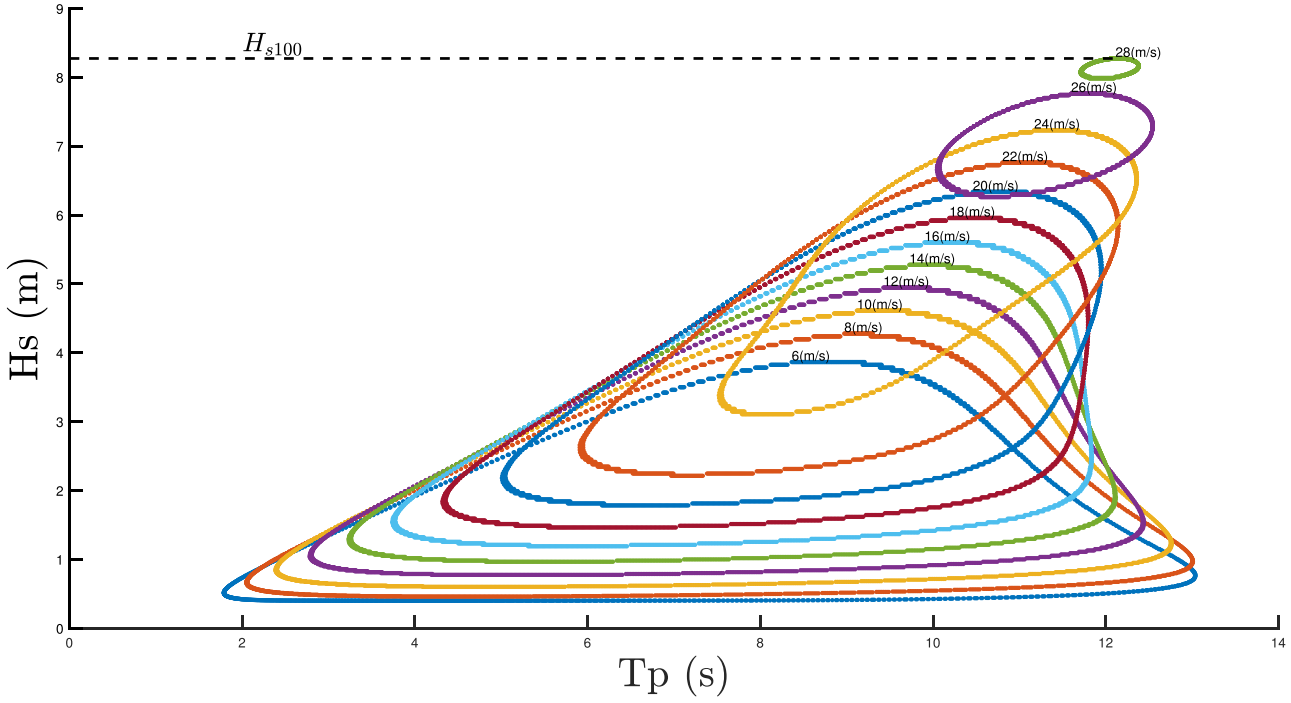
$$W_s = F_{W_s|H_s}^{-1}(\phi(u_3)) \tag{27}$$

The resulting EC is reported in Fig. 6.

After obtaining the 3D environmental contour, it becomes possible to ascertain the utmost extreme event. If we consider a two-dimensional EC based on H_S and T_p, it is typical to test a set of conditions ranging between the maximum Hs and the maximum T_p as detailed in Paduano et al. (2024). However, in this specific EC, higher T_p values lead to a rapid decline in H_s. Furthermore, the maximum period remains near the T_p associated with the maximum H_s. To streamline the testing process and avoid excessive tests related to ULS conditions, a numerical simulation was conducted before the experimental tests. It was observed that the most severe system response, in terms of both motions and tensions, occurs under conditions characterized by the maximum H_s. This sea state was selected as representative of the utmost extreme event. To ensure an accurate statistical representation of this phenomenon, five distinct extreme irregular waves were generated using different seeds. The characteristics of the extreme sea state are reported in Table 11.



(a) 3D environmental contour



(b) Section of the EC at different Wind Speed

Fig. 6. Environmental contour of Lampedusa with a 100 year return period.

4.4. Accidental limit state

In addition to the tests performed in Section 4.3, the system was also assessed in ALS. Four distinct load case scenarios were defined to simulate various failure scenarios, reported in Table 12. In the first configuration (Test ID 154), the system was tested without the forward mooring line in extreme irregular sea state. In the second configuration (Test ID 155), the system was tested without one of the two bow mooring lines in the extreme irregular sea state. In the third configuration (Test ID 156), the system was tested considering the failure of the blade pitch actuator, adding to the system the thrust (generated considering the blade pitch fixed at 0 deg and rigid blades). In the fourth configuration (Test ID 188) the same condition of the test 154 was replicated for the $LCN3$. It should be emphasized that the ALS conditions refer to the

Table 11
Extreme irregular wave.

Wave name	Full-scale		Model-scale	
	H_s (m)	T_p (s)	H_s (mm)	T_p (s)
IW_EX_PR_s01	8.27	12.2	86.2	1.24
IW_EX_PR_s02	8.27	12.2	86.2	1.24
IW_EX_PR_s03	8.27	12.2	86.2	1.24
IW_EX_PR_s04	8.27	12.2	86.2	1.24
IW_EX_PR_s05	8.27	12.2	86.2	1.24

Table 12
ALS load scenarios.

Wave name	Full-scale			Model-scale	
	H_s (m)	T_p (s)	W_s (m/s)	H_s (mm)	T_p (s)
154_*ALS_EX_PR_s04*	8.27	12.2	/	86.2	1.24
155_*ALS_EX_PR_s04*	8.27	12.2	/	86.2	1.24
156_*ALS_EX_s04*	8.27	12.2	28	86.2	1.24
188_*ALS_EX_PR_s04*	8.27	12.2	/	86.2	1.24

Table 13
System identification waves.

Wave Name	$H/\lambda_{w_{\min}}$
MS_CA_Stmax_28	1/28
MS_CA_Stmax_19	1/19
MS_CA_Stmax_14	1/14
MS_CA_Stmax_11	1/11
MS_CA_Stmax_9	1/9

scenario where the fault conditions have already occurred. In this case, the system's response is examined without analyzing what happens at the moment the failure occurs. This aspect will be further investigated in the future and will be the subject of the next experimental campaign.

4.5. System identification waves

To perform the system identification with a limited wave set, several multisine waves with constant amplitude were considered. The multisine waves were designed to have a flat spectrum within the period of interest, which was defined as [0.6, 1.3]. The maximum steepness of the wave train was calculated considering the minimum λ_w. The phase of the multisine waves was defined using the Schroeder method (Kimpián and Augusztinovicz, 2016), such that longer waves are generated before the shorter waves as the wave transport velocity is higher for longer waves. This is done to prevent the overlap of the waves. The signal, lasting 100 s, was repeated 3 times for each test (Table 13).

4.6. Free decays test

In addition to wave-induced tests, free decay tests were conducted to analyze the system's natural oscillations and assess its damping characteristics. These tests provided insights into the system's inherent properties and response in the absence of external excitations. Free decay tests for Heave, Roll, and Pitch were conducted under two different conditions, with and without mooring, while for Surge, Sway, and Yaw free decay tests were conducted only with the mooring system. All the free decays are reported in Table 21.

4.7. Load scenario for additional mooring configurations

Additional experiments are conducted during the campaign to investigate the effects of different pre-tension applied to the mooring system. Four load scenarios, as detailed in Table 14, are selected from the previously described tests and performed to examine the variations in the system's response under different mooring lines pre-tension.

Table 14
Waves tested with different pre-tension values.

Wave name	Full-scale			Model-scale	
	H_s (m)	T_p (s)	W_s (m/s)	H_s (mm)	T_p (s)
IW_OP_05	1.91	6.86	11	19.9	0.70
MS_CA_Stmax_19	/	/	/	/	/
MS_CA_Stmax_11	/	/	/	/	/
IW_EX_PR_s04	8.27	12.2	/	86.2	1.24

5. Experimental setup

The experiments were conducted in Towing Tank 2 of the Ship Hydromechanics Laboratory at Delft University of Technology. The tank measures 85 m in length, 2.76 m in width, and has a maximum water depth of 1.25 m. It is equipped with a flap-type wavemaker at one end, featuring an adjustable virtual hinge point. This mechanism allows the hinge point to be set continuously between the bottom of the tank and infinitely deep, effectively enabling the flap to operate in piston mode. A wave-damping beach is positioned at the opposite end of the tank. For this experimental campaign, the wavemaker was used in piston mode. The water level was set to 1042 mm to match the water depth of 100 m at the project location, scaled to 1:96.

A sketch of the experimental setup for conducting tests in the tank is shown in Fig. 7. This diagram includes the relevant distances between the wave gauges and the prototype, the mooring line anchor points, the positioning of the wind winch, and the overall dimensions of the tank. It is important to note that wave gauge 2 (WG2) is marked with an asterisk (*) to indicate its presence only during the empty tank tests, not when the prototype is in the water. All measurements are referenced to the global system depicted in Fig. 7 and labeled as X_G and Y_G.

A photograph of the actual experimental setup in the test tank is shown in Fig. 8.

In Fig. 9, the block diagram of the entire acquisition system used during the experimental campaign is shown.

Load cells are positioned at the anchor of each mooring line to capture tension data. The wooden plate in Fig. 2b is placed at the bottom of the tank, perforated at the three anchoring points for the secure fastening of three eyebolts. Each eyebolt is connected to a metal clip, to which the load cell is attached. A spring is placed after the load cell, followed by the polyester line. These load cells act as reliable sensors, enabling precise measurement of the tension forces experienced by the mooring lines. Additionally, four wave gauges are installed in close proximity to the model to capture valuable information related to wave elevation, monitoring and analyzing wave characteristics such as amplitude and frequency.

An Optitrack motion tracking system (NaturalPoint, 2023) is employed to accurately measure the motions of the wind turbine device. This setup provides detailed and precise motion data, enabling analysis of the dynamic behavior of the wind turbine under various operating conditions.

The acquisition system incorporates various components for auxiliary purposes. Wave maker input files are generated to simulate different wave scenarios and study their impact on the wind turbine. A trigger signal is implemented to activate an LED light, providing synchronized timing information for specific events during the experiments.

A constant-tension winch (Metsch, 2023) equipped with a load cell is used to apply wind force during the experiments. This setup allows accurate tuning and measurement of the force applied to the wind turbine. The load cell provides real-time readings of the applied wind force. The thrust force is applied as a constant value at the rotor height. The value to be applied is determined, according to the sea state to be tested, by taking the associated value from the thrust curve of the turbine as shown in Figure. The scatter points represent the specific thrust values applied to the winch for each operative irregular sea state in Table 10.

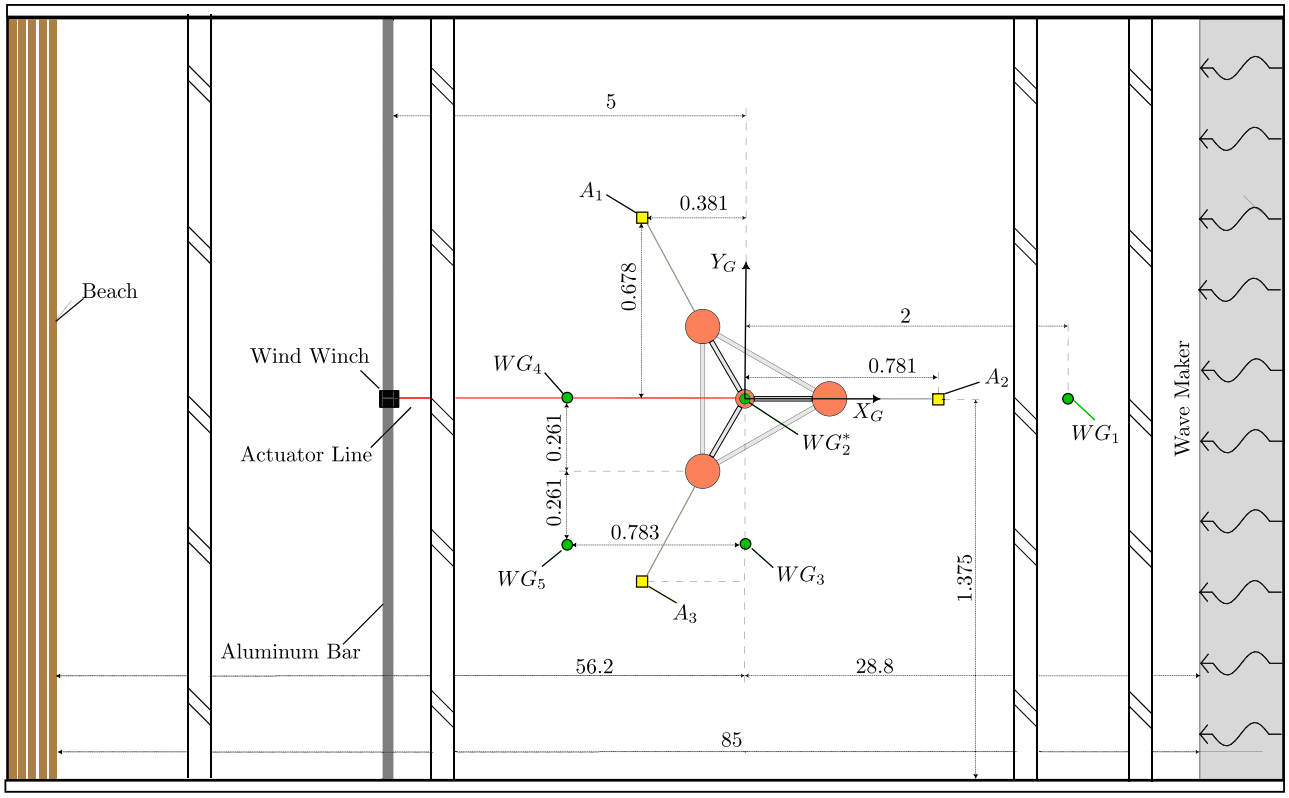


Fig. 7. Graphical representation of experimental setup with Wave Gauges (WG_i), Anchor Points (A_i). The reported distances are expressed in meters.



Fig. 8. Photograph of the experimental setup in the wave tank.

These values are appropriately scaled down to represent the mean thrust observed during time-domain simulations. In the ALS condition, where a failure occurs in the blade pitch controller (Test 156, see Section 6.7), the thrust value is determined through numerical time-domain simulations by locking the rotor and blades. This approach provides a realistic estimation of thrust values across varying wind conditions, enabling the analysis of platform responses under both operational and failure scenarios (Fig. 10).

All the components, including load cells, winch, wave gauges, trigger signal, and wave maker output, are integrated using a National Instruments USB device. This device serves as the central interface for data acquisition, enabling collection and management of the diverse range of signals generated during the experiments. The acquired signals are processed and analyzed on the host PC to extract meaningful insights from the data.

BMCM amplifiers are employed to amplify the signals before they are captured, ensuring the accuracy and reliability of the acquired signals by mitigating potential noise or distortion. The camera system utilized for capturing visual information directly acquires data from the software, which is then saved on the host PC. This comprehensive acquisition system, with its various components working together, facilitates detailed analysis of the wind turbine's behavior under different conditions and provides valuable insights into its performance and response characteristics.

Analog signals, including data from the wave maker, load cells, and wave probes, are recorded at a frequency of 1000 Hz, while those

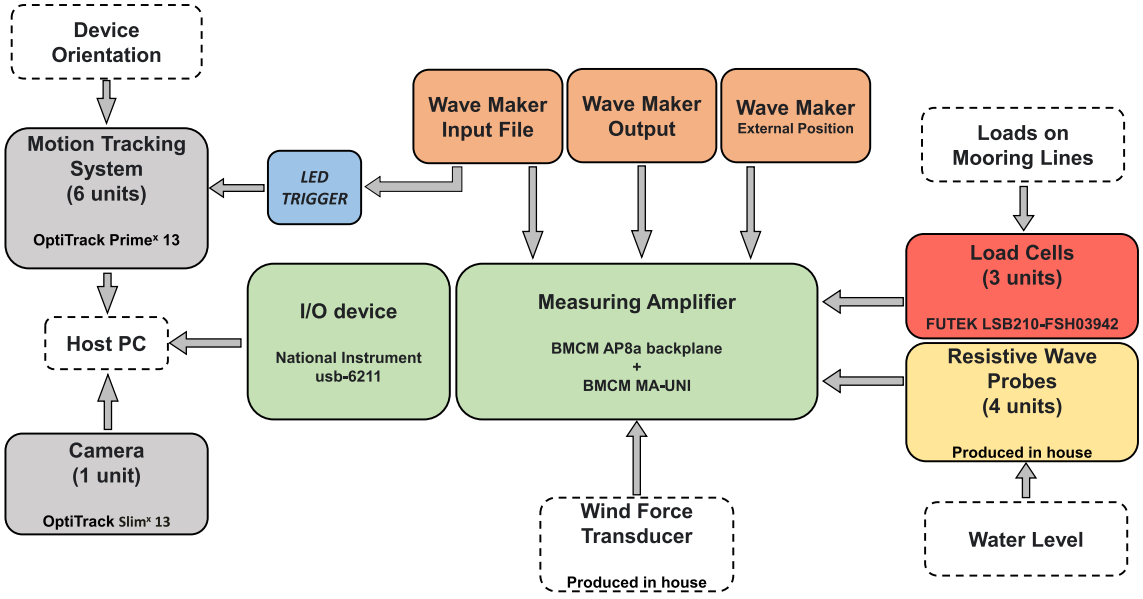


Fig. 9. Acquisition system block diagram.

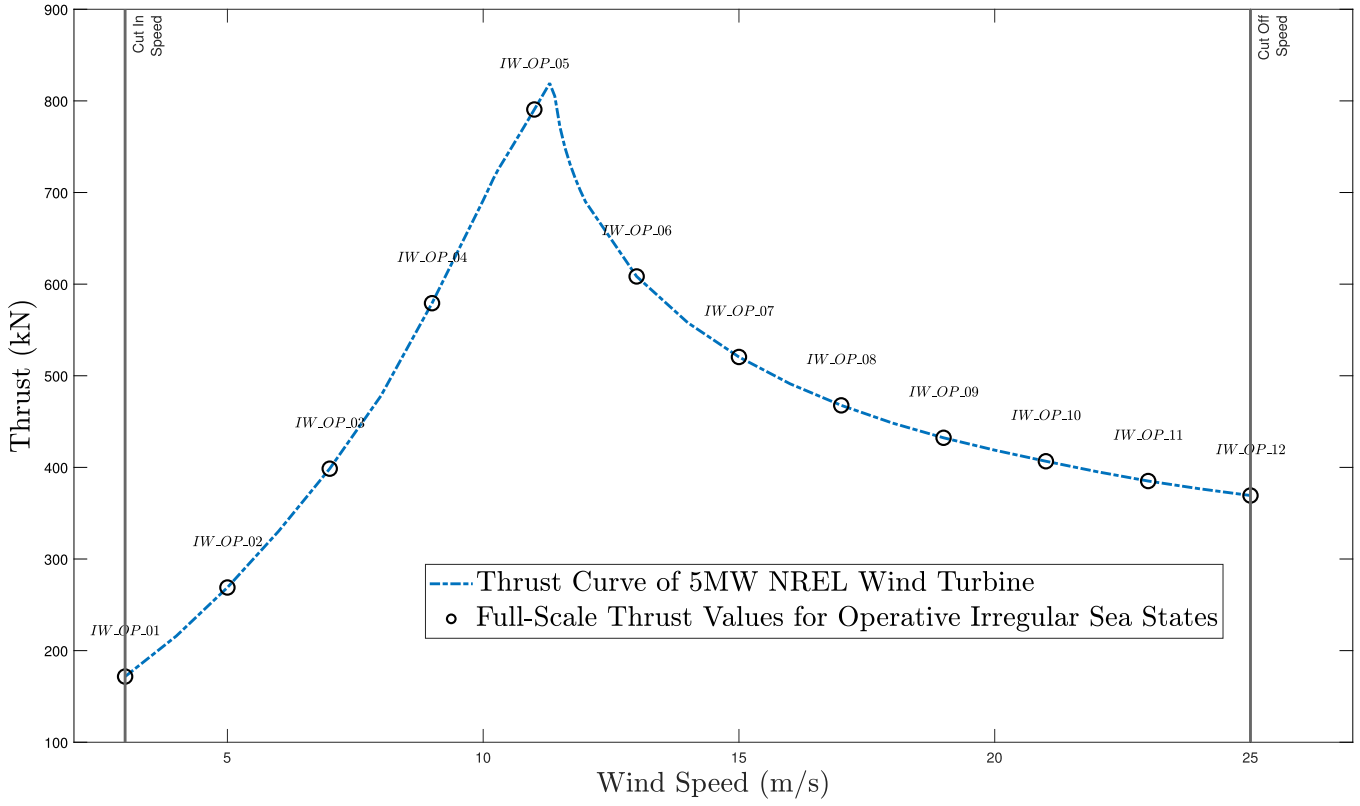


Fig. 10. Thrust curve for the turbine with scatter points indicating thrust values assigned to the winch for each irregular sea state and ALS case.

from the camera system are captured at 100 Hz. Although the acquisition system in LabVIEW records at 1000 Hz, wave-induced dynamic responses do not require such a high sampling rate for accurate analysis. Therefore, data is subsequently interpolated to 100 Hz to align with the camera acquisition rate, ensuring consistency across measurements while maintaining sufficient resolution for capturing dynamic responses. In Fig. 2, the positioning of the markers monitored by the camera system is shown. The output motions from the Optitrack software are referenced to the geometric point monitored by Optitrack (NaturalPoint, 2023), located at a distance $d = [111.75, -4.75, -224.12]$ mm from the substructure's center of gravity. All results presented in the following sections refer to motions relative to the center of gravity after performing the standard rototranslation operations for a rigid body.

6. Experimental results

This section presents the results of the experimental campaign, focusing on assessing the system's response in terms of kinematics and mooring system tensions. The evaluation began with the baseline

Table 15
Free decay tests results, including linear and quadratic damping coefficients (B_{lin} and B_{quad}), resonant period (T_{res}), adjusted coefficient of determination (R^2_{adj}), and sum of squared errors (SSE). B_{lin} and B_{quad} represent the linear and quadratic damping coefficients, respectively. T_{res} indicates the resonant period for each motion type, measured in seconds. R^2_{adj} is the adjusted R^2 value, reflecting the goodness-of-fit of the damping model, while SSE denotes the sum of squared errors, which measures the residuals between observed and fitted values. The table includes tests conducted with mooring (Moor) and without mooring (NoMoor) for various degrees of freedom (DoF) such as surge, sway, heave, roll, pitch, and yaw.

Test ID	Test name	B_{lin} $\left(\frac{\text{N}}{\text{(m/s)}}\right)$	B_{quad} $\left(\frac{\text{N}}{\text{(m/s)}^2}\right)$	T_{res} (s)	R^2_{adj}	SSE
057	*FD_Moor_Surge*	0.10	93.3	10.1	0.978	2.68E−04
061	*FD_Moor_Sway*	0.17	83.7	10.0	0.901	3.23E−04
065	*FD_Moor_Heave*	0.51	287	1.65	0.833	6.27E−02
163	*FD_NoMoor_Heave*	0.24	277	1.81	0.933	6.45E−03
Test ID	Test name	B_{lin} $\left(\frac{\text{Nm}}{\text{(rad/s)}}\right)$	B_{quad} $\left(\frac{\text{Nm}}{\text{(rad/s)}^2}\right)$	T_{res} (s)	R^2_{adj}	SSE
066	*FD_Moor_Roll*	0.04	3.02	2.51	0.860	4.69E−03
069	*FD_Moor_Pitch*	0.06	2.98	2.51	0.303	6.55E−02
074	*FD_Moor_Yaw*	0.06	0.92	6.48	0.913	1.43E−04
168	*FD_NoMoor_Pitch*	0.03	3.47	3.45	0.951	1.56E−03
171	*FD_NoMoor_Roll*	0.03	3.50	3.47	0.943	1.70E−03

configuration, LCS1, and was later extended to various configurations by altering the pre-tension level of the mooring lines.

6.1. Free decay analysis

The free decay tests are conducted to assess the resonant period, linear term, and quadratic term of damping in the system. The evaluation of linear and quadratic viscous damping terms followed the methodology presented in Fontana et al. (2020), which was previously applied to a substructure for a floating offshore wind turbine (FOWT) in Niosi et al. (2023c).

The methodology for calculating damping values starts by examining the system response during free decay test. The objective is to quantify how quickly the system loses energy, which is influenced by both linear and quadratic damping effects.

To analyze this, each oscillation cycle is observed, and the amplitudes of successive peaks in the decay are measured. By calculating the logarithmic decrement (the rate of decrease in amplitude between consecutive peaks) it is possible to estimate the effective damping for each cycle. This decrement provides insight into the total damping force acting on the system, which includes contributions from both linear and quadratic damping.

To distinguish between these linear and quadratic components, the effective damping coefficient is plotted against the mean amplitude of each cycle. This creates a set of points representing how damping varies with amplitude. A linear regression is then applied to this data, fitting a line to capture the trend. The intercept and slope of this line provide the linear and quadratic damping coefficients, respectively.

As shown in Table 15, the linear damping term remains very small compared to the quadratic term in all tests, indicating that non-linear viscous effects are the main contributors to damping. The impact of the mooring system on the response of the device was observed by comparing the results of free decay tests conducted with and without mooring. The tests revealed that the resonant period in pitch and roll with mooring was shorter than without mooring, which can be attributed to the increased stiffness introduced by the mooring system. Additionally, damping values were modified as they depend on the motion frequency.

Results from the free decay analysis indicate a reasonably good fit across most degrees of freedom (DoF), except in the case of the pitch free decay test with mooring. In this case, a less accurate fit can be attributed to coupling between pitch and surge, which is introduced through the mooring system. This coupling effect occurs because the pitch free decay motion also excites surge motion, complicating the damping fit for pitch with mooring. In contrast, the coupling of roll with sway did not impact the test results because sway motion was controlled and minimized during the roll tests, isolating the response of roll effectively. The calculated damping values for roll align closely with expectations, consistent with similar damping values obtained for roll.

The goodness-of-fit was evaluated using the adjusted coefficient of determination (R^2_{adj}) and the sum of squared errors (SSE), as reported in Table 15. For clarity, the table includes abbreviations for key parameters and methods used. The calculation of the damping coefficient followed the methodology by Fontana et al. (2020), incorporating specific formulations for the linear and quadratic viscous damping terms. The experimentally identified viscous damping terms obtained in this analysis are important for numerical validation, as they can be integrated into potential flow numerical software to enhance the estimation of low-frequency motions for the floating structure.

6.2. RAO in regular, irregular, and multisine waves

To provide a concise analysis of the experimental findings presented in Tables 22, 23 and 25, a frequency domain analysis was conducted by constructing the RAOs for tests conducted under regular, irregular, and multisine wave conditions. The process for constructing the RAOs under regular wave conditions followed these steps:

- Temporal data from all acquisition channels (motions, tensions, wave elevation, trigger, wave maker position) is processed by removing the transient phase of the test and using a periodic signal.
- The Single Side Spectrum Amplitude (SSSA) of the trimmed signal is calculated to extract the amplitude of the main harmonics.
- The same procedure is applied to the empty-tank wave conditions corresponding to the regular wave tests, and the amplitude of the main harmonic in the signal associated with WG2, where the device is located, is calculated.
- RAOs were then constructed by dividing the amplitude of the wave frequency main harmonic for surge, heave, and pitch motions, as well as the tensions in the three mooring lines, by the wave amplitude obtained from the Fast Fourier Transform (FFT) of the empty WG2 test.

The procedure used to obtain the RAOs in regular waves has been reported in Eq. (28) and detailed in Niosi et al. (2023a):

$$RAO_i = \frac{FFT(S_i(t_{trimmed}))|f_w}{FFT(WG2(t_{trimmed})|f_w} \tag{28}$$

in which S_i is the chosen signal which can vary among Surge, Heave, and Pitch motions and Mooring Line 1, 2, and 3 tension. $FFT(S_i(t_{trimmed}))|f_w$ is the value of the FFT applied on the trimmed Signal at wave frequency

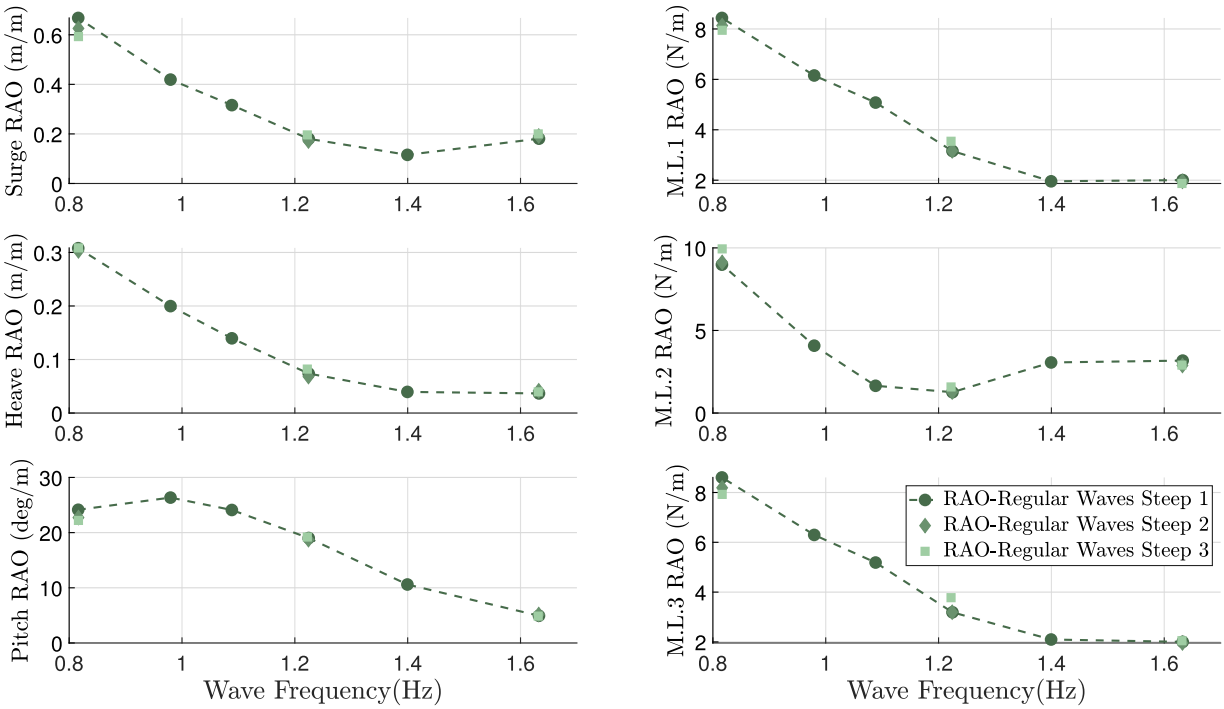


Fig. 11. Experimental RAOs in regular waves obtained with tests reported in Table 22.

(f_w). $FFT(WG2(t_{trimmed}))|f_w$ is the value of the FFT applied on the WG2 trimmed time history acquisition calculated at wave frequency. It should be noted that the set of regular waves used in the analysis includes waves with three different steepness levels, as shown in Fig. 11. From the figure, it can be observed that there is not a significant variation in the RAOs as the wave steepness changes, indicating a linear behavior of the floating structure.

To calculate the RAOs in irregular waves, the following procedure is followed:

- The time-domain signals from different acquisition channels are initially trimmed to exclude any transient effects. Then, FFT is applied to both the acquired signal and the wave elevation signal from empty tank tests, resulting in the Single-Sided Spectral Amplitude (SSSA) of each signal.
- To ensure that the frequency vectors of the FFT outputs from the acquired signal and the wave elevation match, both signals must be sampled over the same time period, resulting in FFT vectors of equal length.
- Prior to dividing the SSSA values, a smoothing process is applied to reduce numerical noise. Specifically, Gaussian smoothing is used with a window of 41 samples. A sensitivity analysis (see Appendix A, Fig. 27) was conducted to determine the optimal window size, balancing noise reduction with accurate system response representation.
- The RAOs are then computed by dividing the smoothed SSSA of the wave elevation by the smoothed SSSA of the acquired signal. The frequency bandwidths for each test vary slightly to accommodate slight shifts in the peak frequencies of the irregular waves, which affect the energy distribution in the experimental wave spectrum.
- After obtaining the RAO for each tested wave condition, we calculate the AETFE (Averaged Experimental Transfer Function Estimate), which represents the system's average response across different wave frequencies and wind conditions (see Fig. 12). The AETFE is calculated as a mean over the tested wave conditions:

$$AETFE(w) = \frac{\sum_{i=1}^{N_{\text{waves}}} RAO_i(w)}{N_{\text{waves}}} \tag{29}$$

where:

$$RAO_i(w) = \frac{\text{FFT}(S_i(t))}{\text{FFT}(\eta_{wave_i}(t))} \tag{30}$$

Here, N_{waves} represents the number of individual wave conditions tested. Each $RAO_i(w)$ corresponds to a different tested wave condition, and the AETFE is effectively the mean RAO across these conditions, providing a robust average response of the system across varying wave states.

The calculation of the AETFE for multisine waves follows the same procedure used for irregular waves, with the difference being that, while in irregular waves, the frequency band used for constructing the individual RAO varies depending on the peak wave period, in this case, the frequency band is constant. This is because the frequency spectrum of multisine waves is a rectangular box with a constant amplitude ranging from 0.8 to 1.8 Hz as shown in Fig. 13.

In Fig. 14 we present a comparison of the RAOs using three types of waves. Firstly, it is important to note that for irregular waves, which represent the operating conditions of the structure, a constant wind force is applied through an actuator line. The thrust values are the design values provided in document (Jonkman et al., 2009) for the NREL turbine. In Fig. 14, it can be observed that the differences between the three RAOs are practically negligible, indicating that if the stiffness of a taut-mooring is constant, the dynamic operating conditions of the structure are not dependent on the incident wind on the turbine. Conversely, as seen in Fig. 15, wind forces primarily and noticeably impact the average values of surge and mooring tensions. A strong correlation between the mean surge and mean tension in the mooring system can be observed. The maximum mean surge corresponds to the MOSS condition, which underlines that the thrust force is more impactful with respect to the mean drift force on mean Surge and mean tension values. In the same figure, it can be seen how, for system ID waves, the average values of surge are much lower, despite the initial pre-tension of the mooring lines being the same as that of the irregular waves. This confirms that the mean drift forces have a reduced effect compared to the thrust, as in this case, they are the only forces acting on the moored structure.

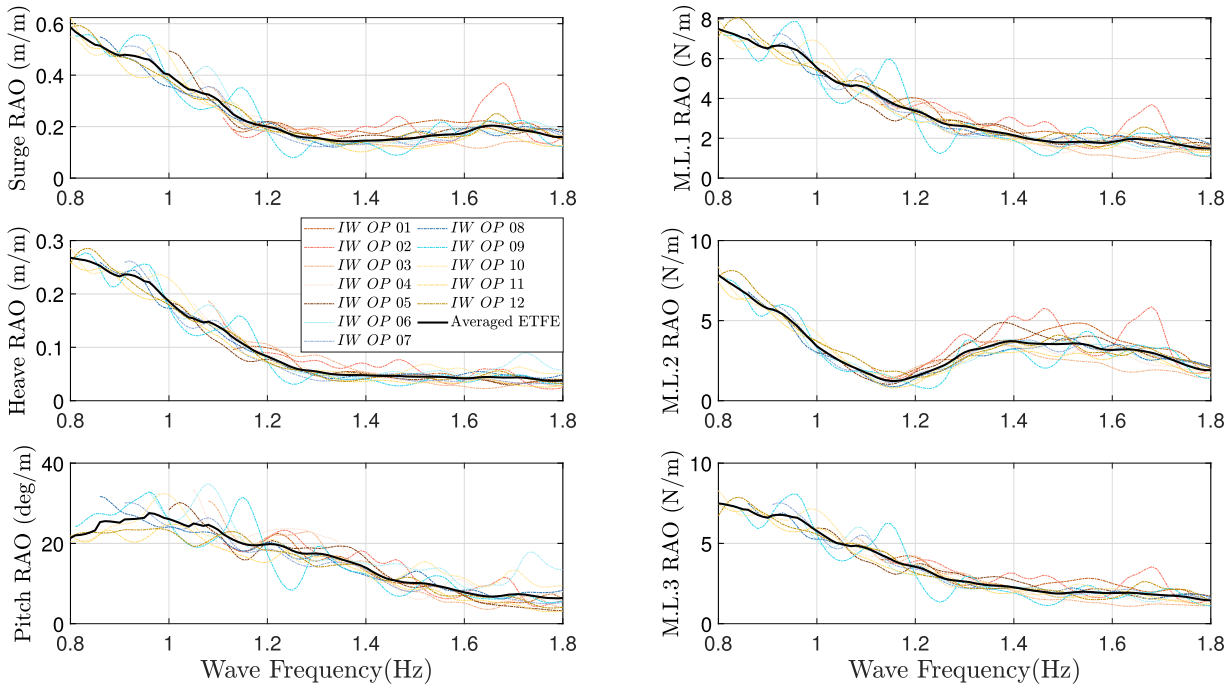


Fig. 12. AETFE: irregular waves obtained considering tests with ID from 95 to 106 and 128, reported in Table 23.

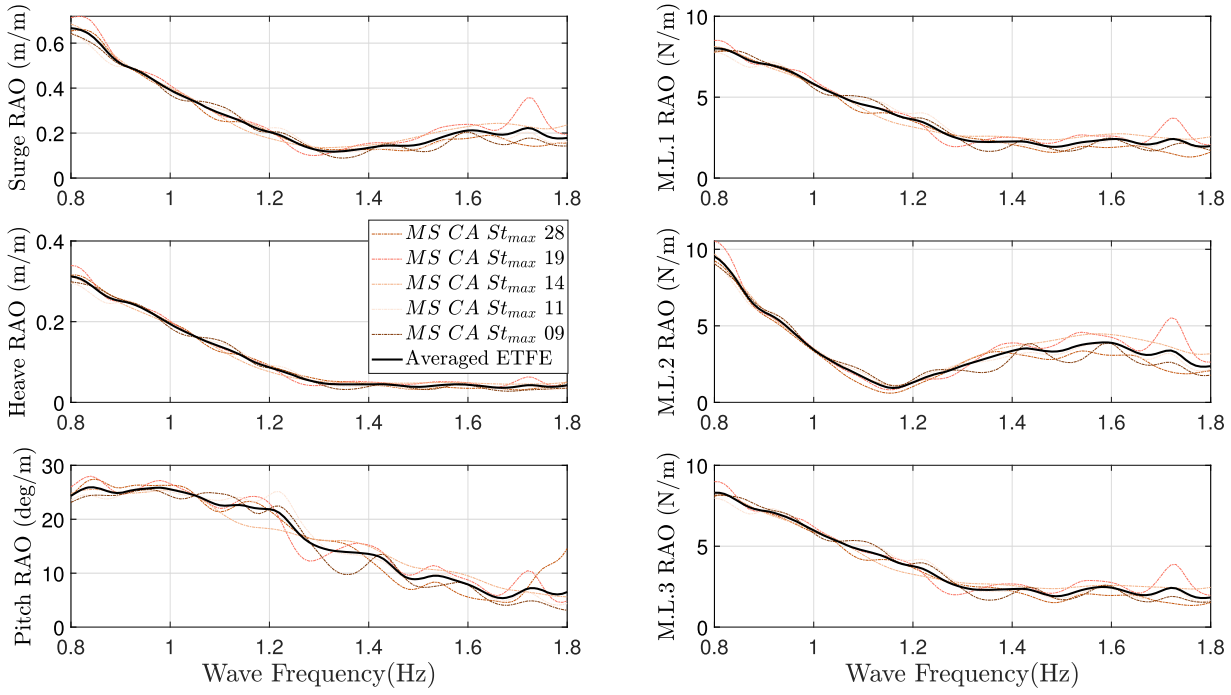


Fig. 13. AETFE: multisine waves obtained with tests reported in Table 25.

6.3. Repeatability analysis

In this section, the repeatability of the conducted analyses is assessed. Specifically, the irregular operational wave with maximum thrust has been chosen as the test case to be repeated 10 times. The test conditions remain consistent to ensure the most coherent result possible. Generally, when conducting a repeatability analysis, a physical quantity acquired by the sensor is selected (ITTC, 2014). In this case, H_s and T_e of the wave gauges have been considered as parameters of the repeatability analysis. The results are presented in Fig. 16. In general, the normalized standard deviation is 1.1 % for H_s and 0.3 % for T_e regarding Wave Gauge 1, indicating a faithful reproduction of the generated wave. It's important to note that there is a difference in wave height readings among the various wave gauges. This difference is attributed to the diffraction and radiation phenomena of the prototype.

Additionally, the RAOs of the system were evaluated following the methodology for irregular waves described in Section 6.2. Fig. 17 illustrates the RAO of the device for each conducted test, the average response, and a $\pm 3\sigma$ confidence interval calculated for each frequency. In general, it can be affirmed that the results of the repeatability

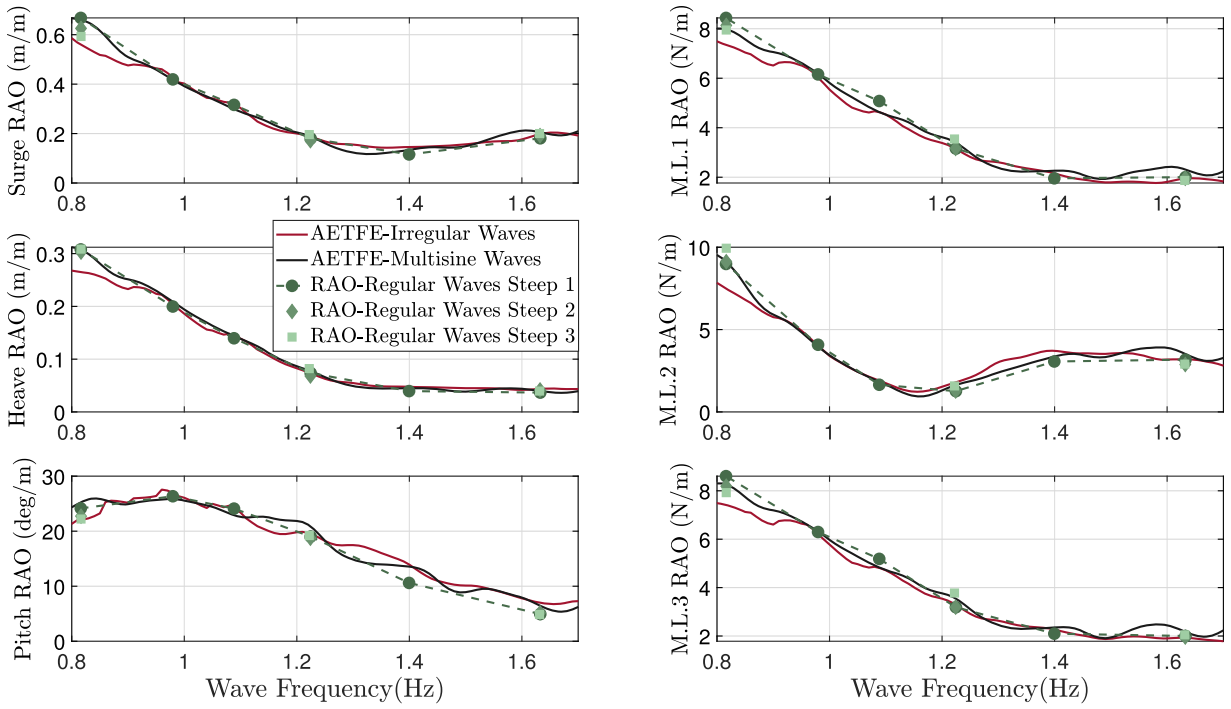


Fig. 14. Experimentral RAO in regular waves, AETFE in irregular and multisine waves.

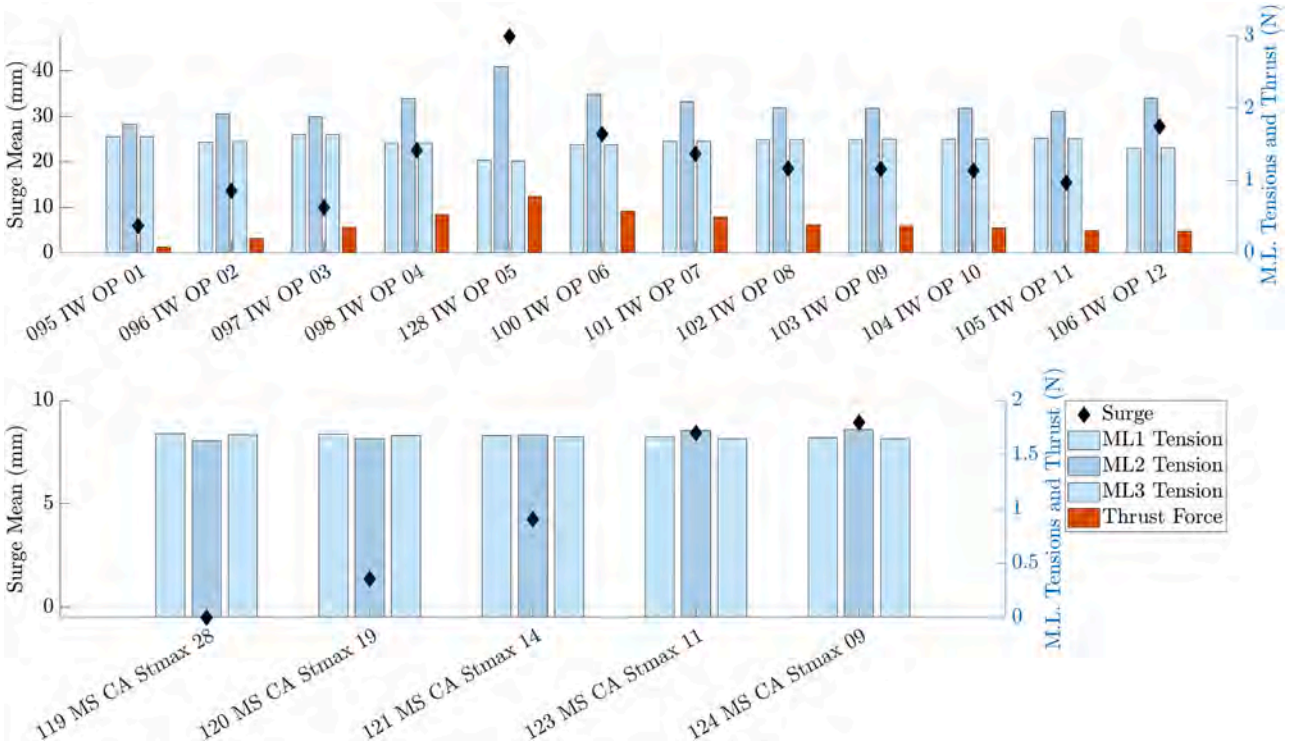


Fig. 15. Mean values of surge, mooring lines tension, and thrust force.

analysis are favorable, highlighting the ability of the experimental setup to faithfully reproduce data, both in terms of the generated wave and the device response.

6.4. *Maximum operative sea state: pre-tension effect*

The dynamic response of the system under varying levels of pre-tension is illustrated in the RAO plots (Fig. 18) for surge, heave, pitch, and mooring line tensions (ML1, ML2, and ML3) across different wave frequencies, as well as in the bar plot (Fig. 19), which shows the average surge displacement and mooring line tensions for each load case. The load cases are organized by pre-tension level in the following order: LCS5 > LCS1 > LCS2 > LCS3 > LCS4, with LCS5 representing the highest pre-tension.

The RAO plots indicate that changes in pre-tension have a limited effect on the kinematic responses of the system (surge, heave, and pitch).

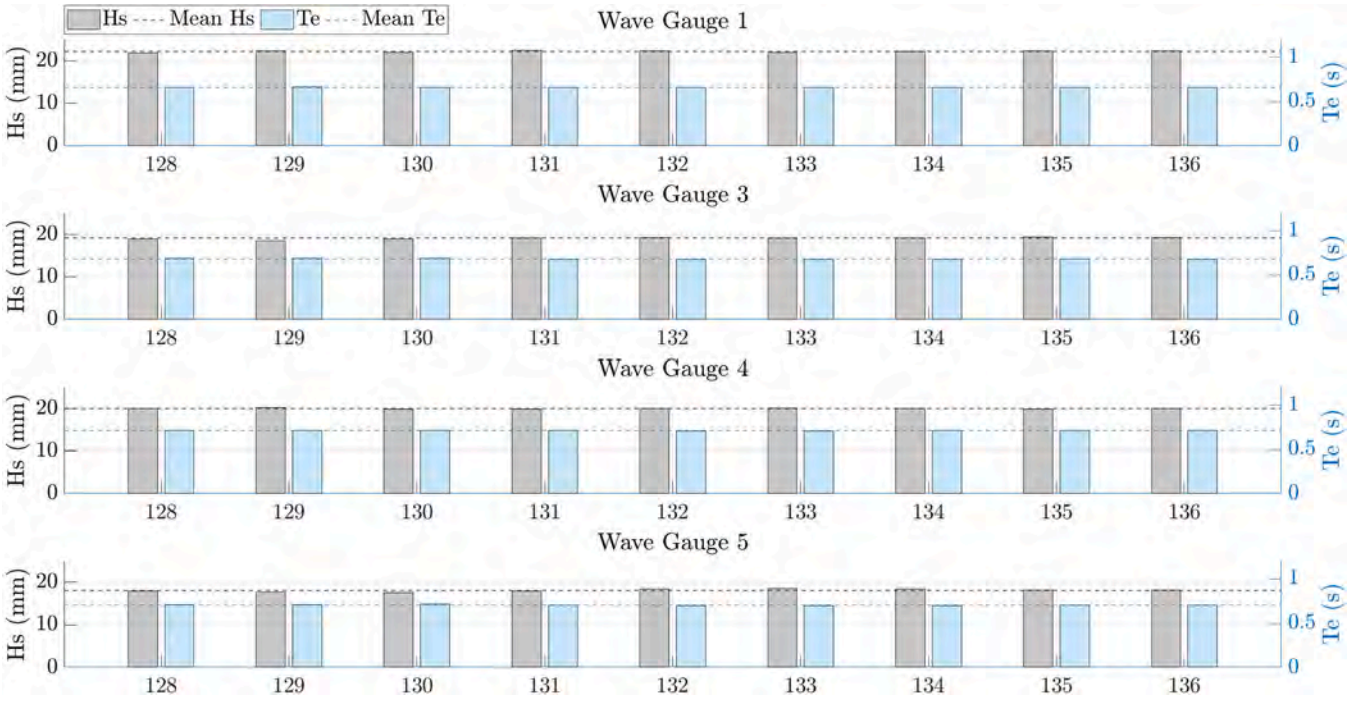


Fig. 16. Repeatability test results on wave gauges acquisitions obtained considering tests with ID from 128 to 136, reported in Table 23.

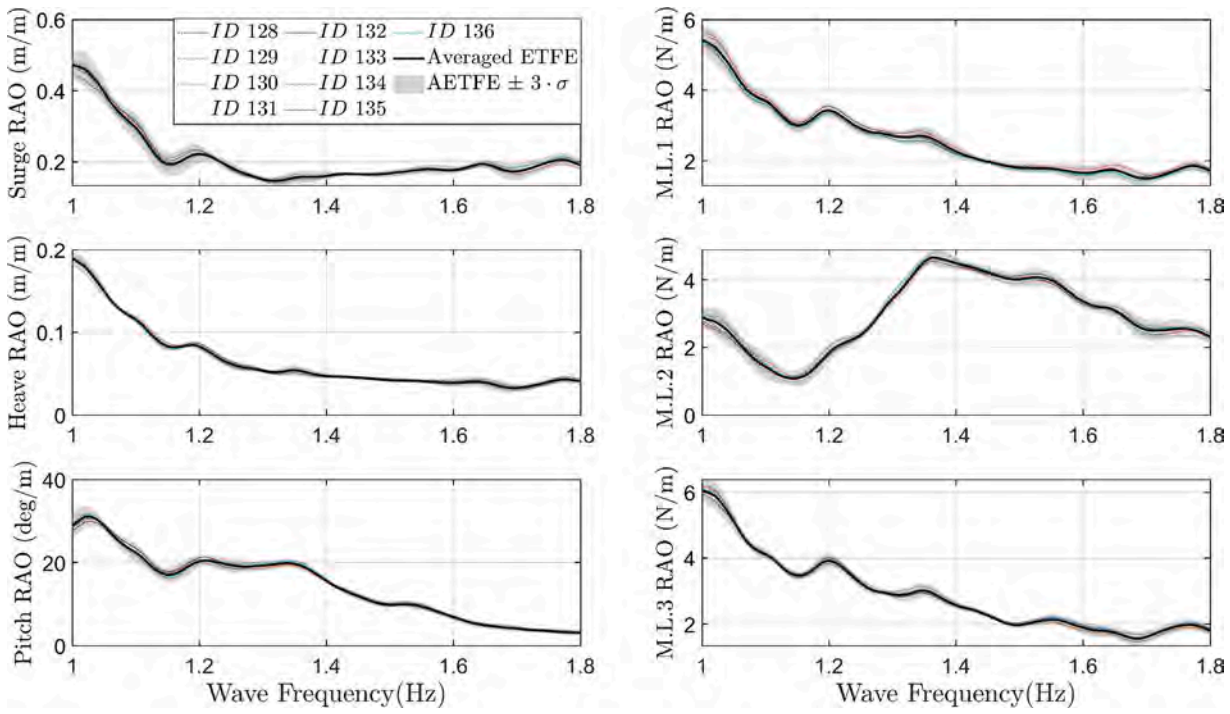


Fig. 17. AETFE: repeatability tests obtained considering tests with ID from 128 to 136, reported in Table 23.

Surge and heave responses peak around 1.0 Hz and then decrease as the frequency increases, showing minimal variation across load cases. This stability suggests that changes in pre-tension do not significantly impact the overall movement of the system in surge and heave. In the pitch RAO, slight differences can be observed, with LCS5, the case with the highest pre-tension, showing a marginally different response. This indicates a minor influence of pre-tension on pitch dynamics.

In contrast, the RAO plots for the mooring line tensions (ML1, ML2, and ML3) demonstrate a noticeable impact of pre-tension. Higher levels of pre-tension lead to consistently higher RAO values for the tensions in the mooring lines, especially around 1.0 Hz. This effect is particularly pronounced in ML2, where increased pre-tension amplifies the dynamic response, suggesting that load distribution among the mooring lines is sensitive to changes in pre-tension.

The bar plot (Fig. 19) provides additional insights, showing average surge displacement and average mooring line tensions for each test. Surge displacement is higher in cases with lower pre-tension (e.g., LCS4 and LCS3) and decreases as pre-tension increases, with

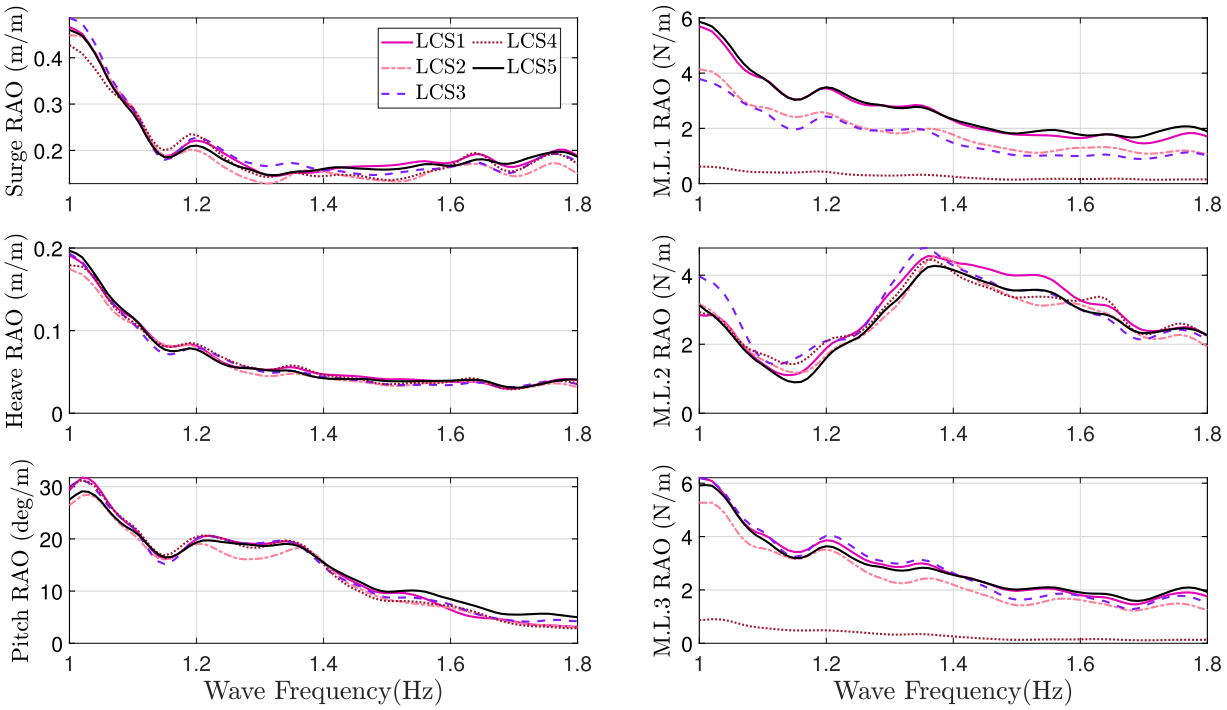


Fig. 18. MOSS RAO: pre-tension levels. Results obtained considering tests with ID 128 144 149 157 199 178 180 189, reported in Tables 23 and 26.

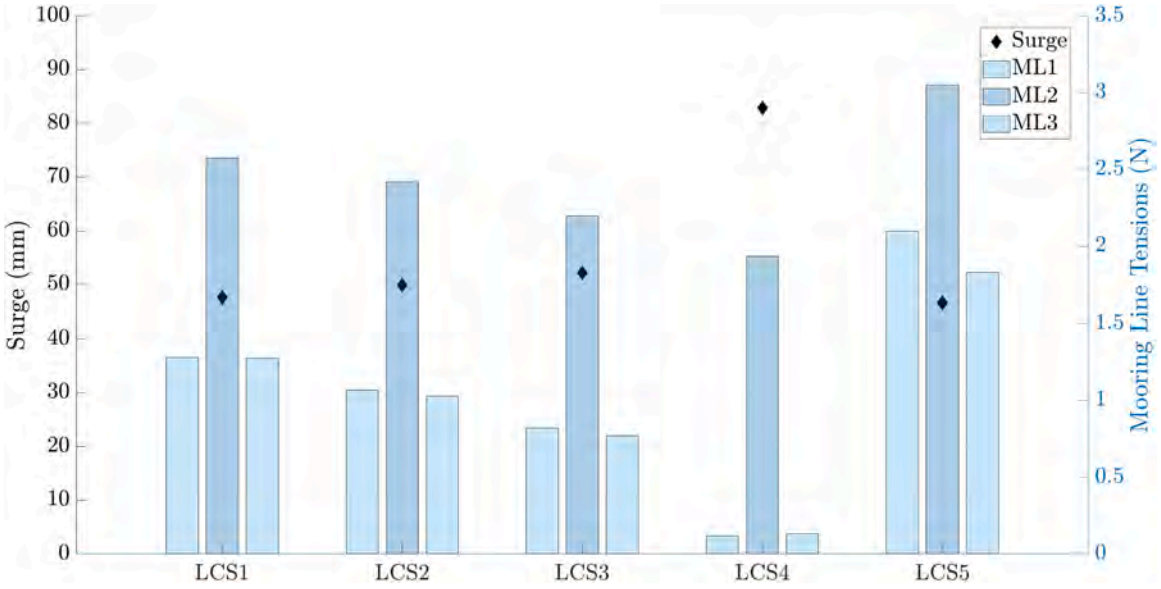


Fig. 19. Mean value of surge and mooring lines tension. Results obtained considering tests with ID 128 144 149 157 199 178 180 189, reported in Tables 23 and 26.

the lowest surge value observed in LCS5. This trend suggests that higher pre-tension contributes to stabilizing the horizontal motion of the structure by reducing surge displacement. Conversely, the average tension in each mooring line increases with higher pre-tension levels, with the highest values observed in LCS5 for all three mooring lines.

In summary, pre-tension has a significant effect on both surge displacement and mooring line tensions. Higher pre-tension levels reduce the average surge displacement, contributing to increased stability of the structure, but also lead to greater loads in the mooring lines. This dual effect highlights the importance of carefully balancing pre-tension to manage both the motions of the structure and the loads experienced by the mooring lines, which is essential for ensuring system stability and protecting the integrity of the mooring lines under operational conditions.

6.5. *Multisine waves: pre-tension effect*

In this subsection, we present the results obtained from multisine wave tests conducted under different pre-tension configurations, following the methodology outlined in Section 6.2. Unlike the case described in Section 6.4, these tests do not include turbine thrust load; only hydrodynamic loads associated with the multisine wave spectrum, as defined in Section 6.5, are considered.

The RAO plots in Fig. 20 illustrate the dynamic response of the system under these conditions. Overall, variations in pre-tension levels

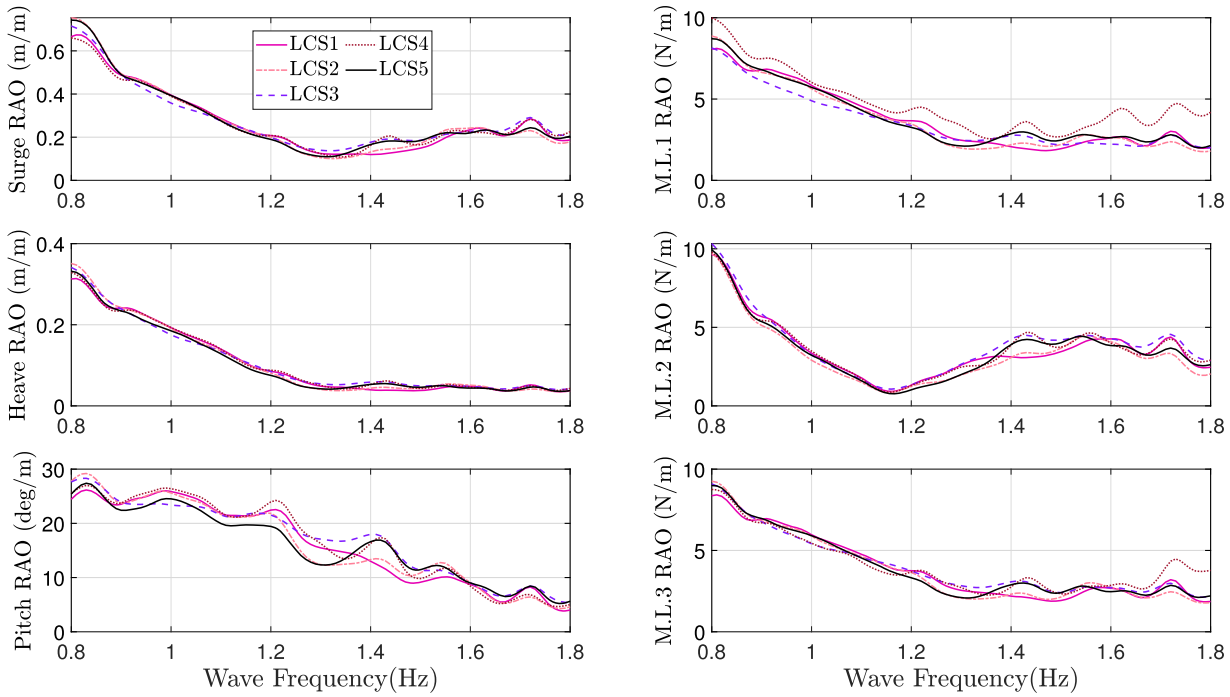


Fig. 20. Multisine RAO: pre-tension levels. Results obtained considering the mean RAO of multisine wave $MS_CA_Stmax_19$ and $MS_CA_Stmax_11$.

have limited influence on the dynamic response of the system, both in terms of motions (surge, heave, and pitch) and mooring line tensions (ML1, ML2, and ML3). This indicates that the absence of thrust allows the wave-induced hydrodynamic forces to dominate the response.

In terms of motions, the RAO curves for surge, heave, and pitch show only minor differences across the pre-tension levels (LCS1 through LCS5), suggesting that pre-tension adjustments have minimal impact on these motion responses. The surge and pitch RAOs maintain a stable profile, peaking around 1.0 Hz and then decreasing with higher frequencies.

The tension RAO plots for mooring lines ML1, ML2, and ML3 reveal some interesting trends in the absence of thrust. Lines ML1 and ML3 exhibit a higher RAO response compared to the case with thrust (Fig. 18), indicating that without the stabilizing effect of thrust, these lines are subjected to greater dynamic tension fluctuations. This effect is most evident at frequencies around 1.0 Hz, where the RAO peaks for ML1 and ML3 are more pronounced.

In contrast, the behavior of ML2, the bow line that typically experiences direct influence from turbine thrust, changes markedly in this scenario. Without the thrust force, ML2 shows a reduction in RAO values compared to the thrust-loaded case, showing that an increase in the average tension value of mooring lines reduces the dynamic components of the tension.

In summary, while pre-tension variations have a limited effect on the overall motion dynamics of the system, the absence of turbine thrust leads to noticeable changes in mooring line tensions.

6.6. Ultimate limit state (ULS) analysis: pre-tension effect

In this subsection, a comparison is presented between different configurations of the mooring system, focusing on surge motion, pitch, and the tensions in the mooring lines. The analysis considers the system response to an extreme irregular wave condition, which excites the structure within a frequency range from 0.7 Hz to 1.2 Hz. The FFT was applied to examine the response amplitude across various frequencies. The comparison was conducted using the extreme irregular sea state $IW_ND_EX_s04$.

Unlike previous analyses where RAO plots were used, the Figures in this section display the direct amplitude of the response as a function of frequency. Fig. 21 shows the surge amplitude response across the frequency range for each mooring configuration, revealing a consistent response pattern across different pre-tension levels. Small variations are observed in the primary wave frequency range, indicating that the system response remains stable regardless of the pre-tension configuration.

However, at lower frequencies, small variations appear. Specifically, as pre-tension in the mooring lines increases, the resonant frequency of the surge shifts slightly towards higher frequencies, ranging from approximately 0.08 Hz to 0.11 Hz. This shift can be attributed to changes in the surge mooring stiffness term (K_{11}) induced by varying pre-tension levels. The FFT analysis also shows an absence of significant coupling between surge and pitch motions, suggesting that the coupling term (K_{15}) in the stiffness matrix has a minimal effect on the system response.

In Fig. 22 is reported the frequency response amplitude of Pitch. A strong coupling between Pitch and Surge is observed, indicating a significant value of the coupling term (K_{51}) in the stiffness matrix. Also, in the wave frequencies, the response of the system is consistent across different pre-tension. The behavior of the Pitch at low frequencies exhibited similarities to Surge. Increasing the pre-tension in the mooring system causes a shift in the peak to higher frequencies. Also, with higher pre-tension, the peak is reduced in amplitude because the coupling term (K_{51}) is reduced with higher pre-tension. The resonant frequency of Pitch remained almost constant at 0.4 Hz, attributed to the constant geometrical stiffness (K_{55}) in Pitch.

In Fig. 23 is reported the FFT of Heave. At low frequency, the response is null, indicating as expected that Heave and Surge are completely decoupled. The response is consistent across all frequencies, suggesting no impact of the pre-tension of the mooring system on heave. The resonant frequency in this configuration is 0.59 Hz, which is consistent with the results found in the free decay tests.

The tensions in the mooring system are influenced by surge, heave, and pitch motions. Fig. 24 shows a relatively consistent response across the entire frequency range, with noticeable differences primarily at the surge resonance frequencies, where the geometrical stiffness K_{11} varies due to different pre-tension levels. However, because the surge resonance frequency lies well outside the wave spectrum, changes in K_{11} have a limited effect on the amplitude of the response. In contrast, the

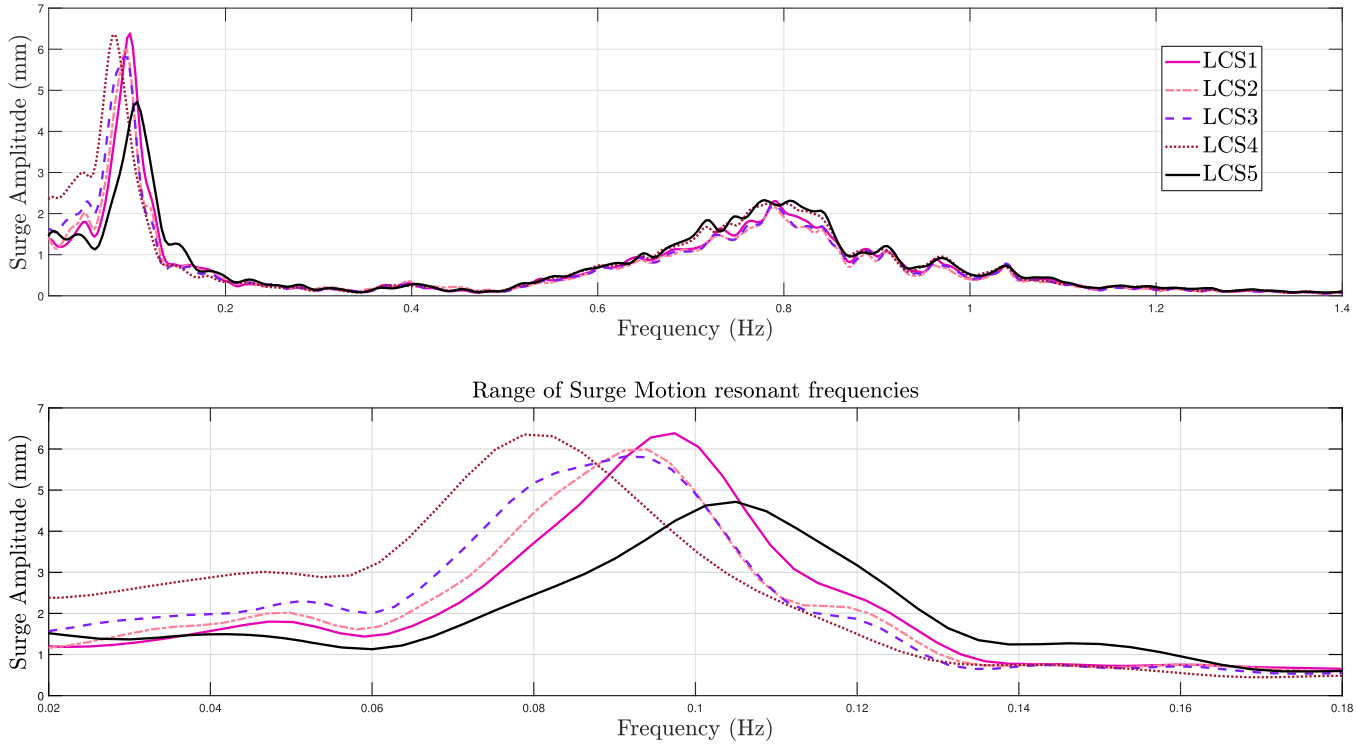


Fig. 21. ULS analysis: surge frequency response with different pre-tension levels. Zoom in the range of Surge motions natural frequency. Results obtained considering tests with ID 117 147 152 160 198, reported in Tables 24 and 26.

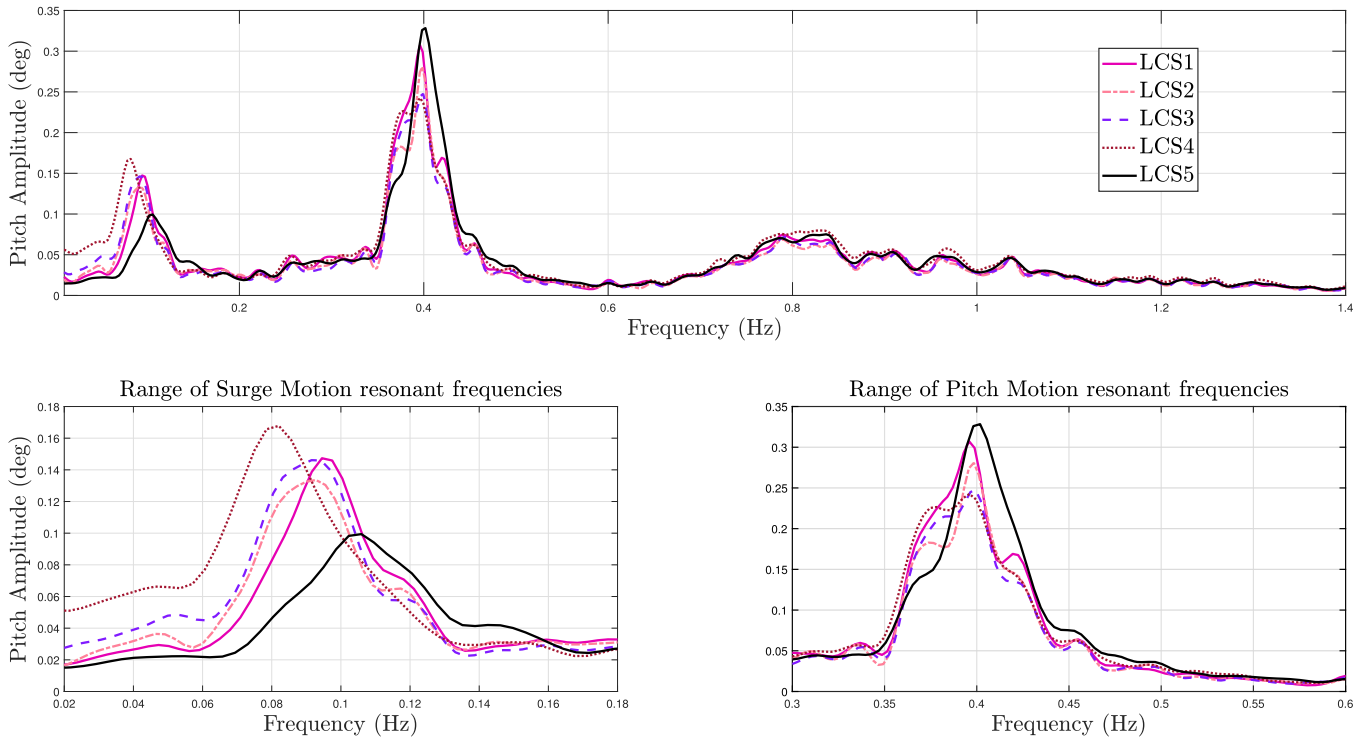


Fig. 22. ULS analysis: pitch frequency response with different pre-tension levels. Zoom in the range of Surge and Pitch motions natural frequencies. Results obtained considering tests with ID 117 147 152 160 198 reported in Tables 24 and 26.

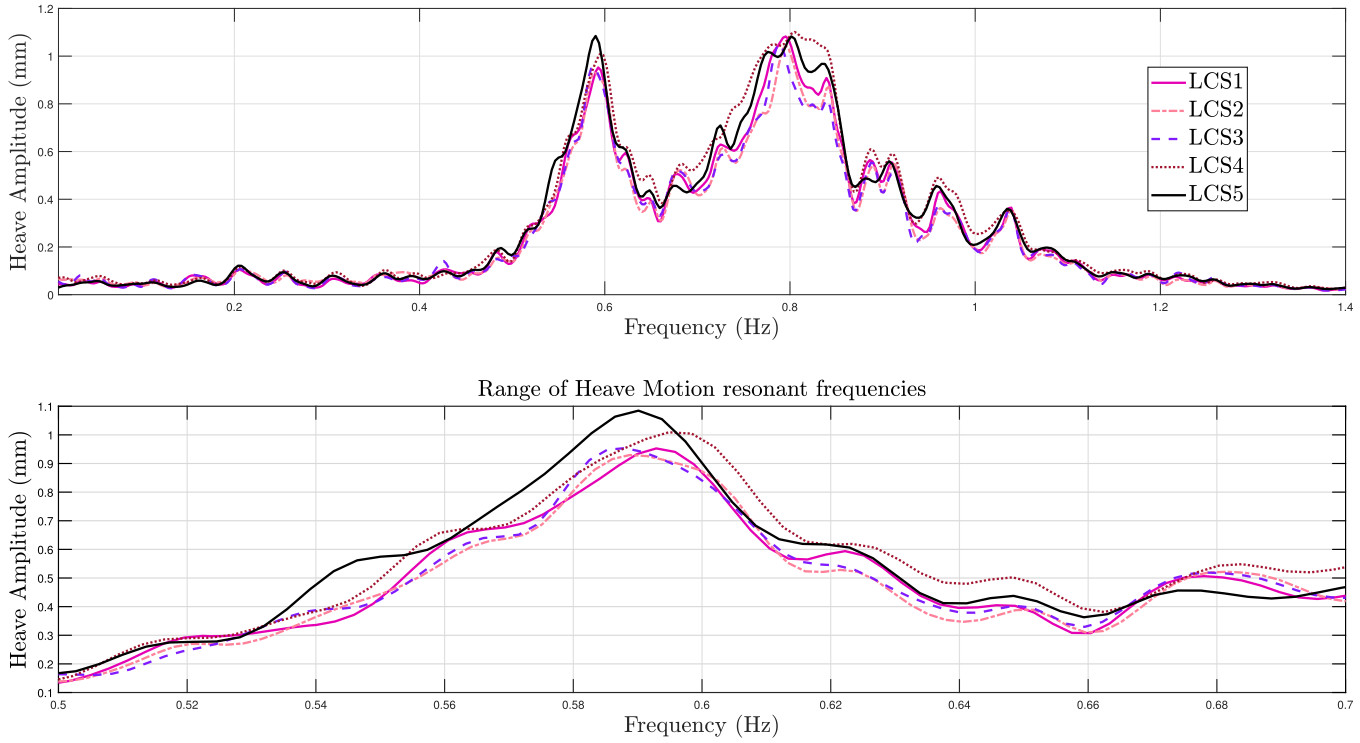


Fig. 23. ULS analysis: heave frequency response with different pre-tension levels. Zoom in the range of Heave motions natuaral frequency. Results obtained considering tests with ID 117 147 152 160 198, reported in Tables 24 and 26.

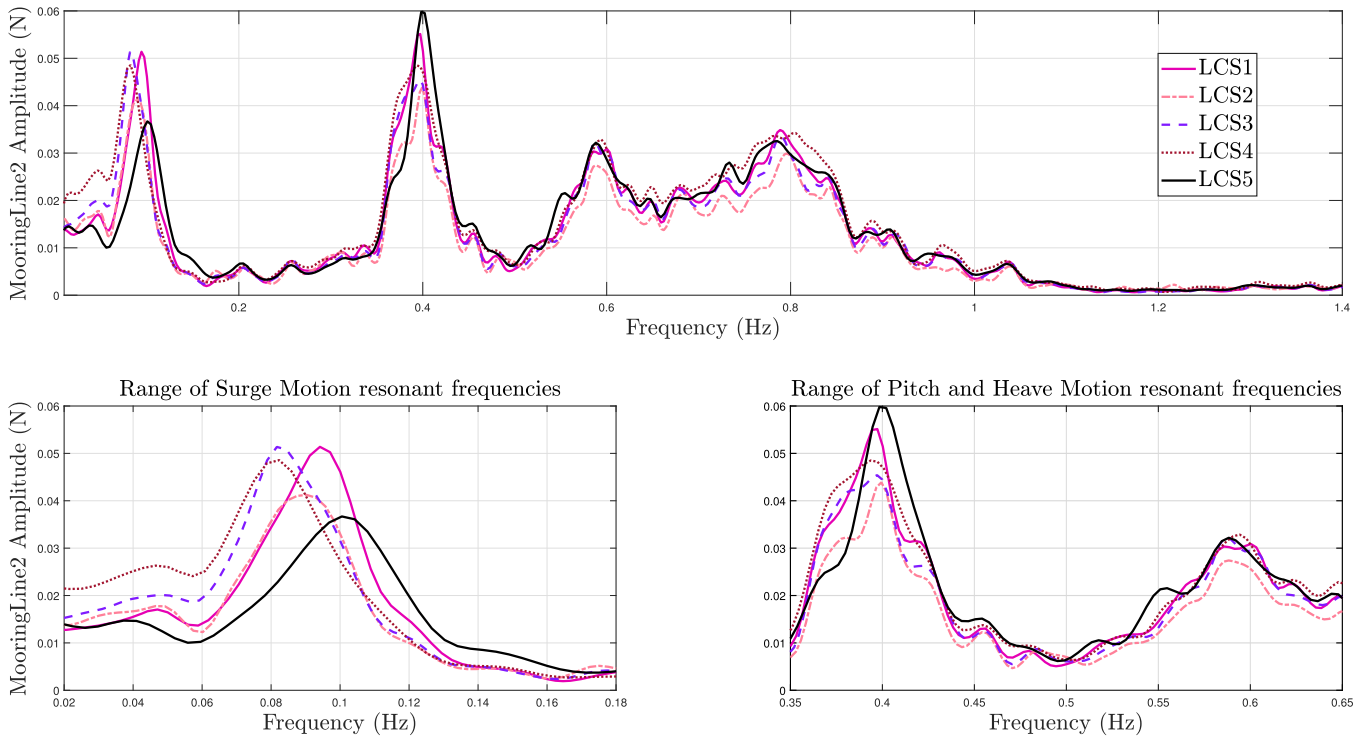


Fig. 24. ULS analysis: mooring Line 2 frequency response with different pre-tension levels. Zoom in the range of Surge and Pitch motions natural frequencies. Results obtained considering tests with ID 117 147 152 160 198, reported in Tables 24 and 26.

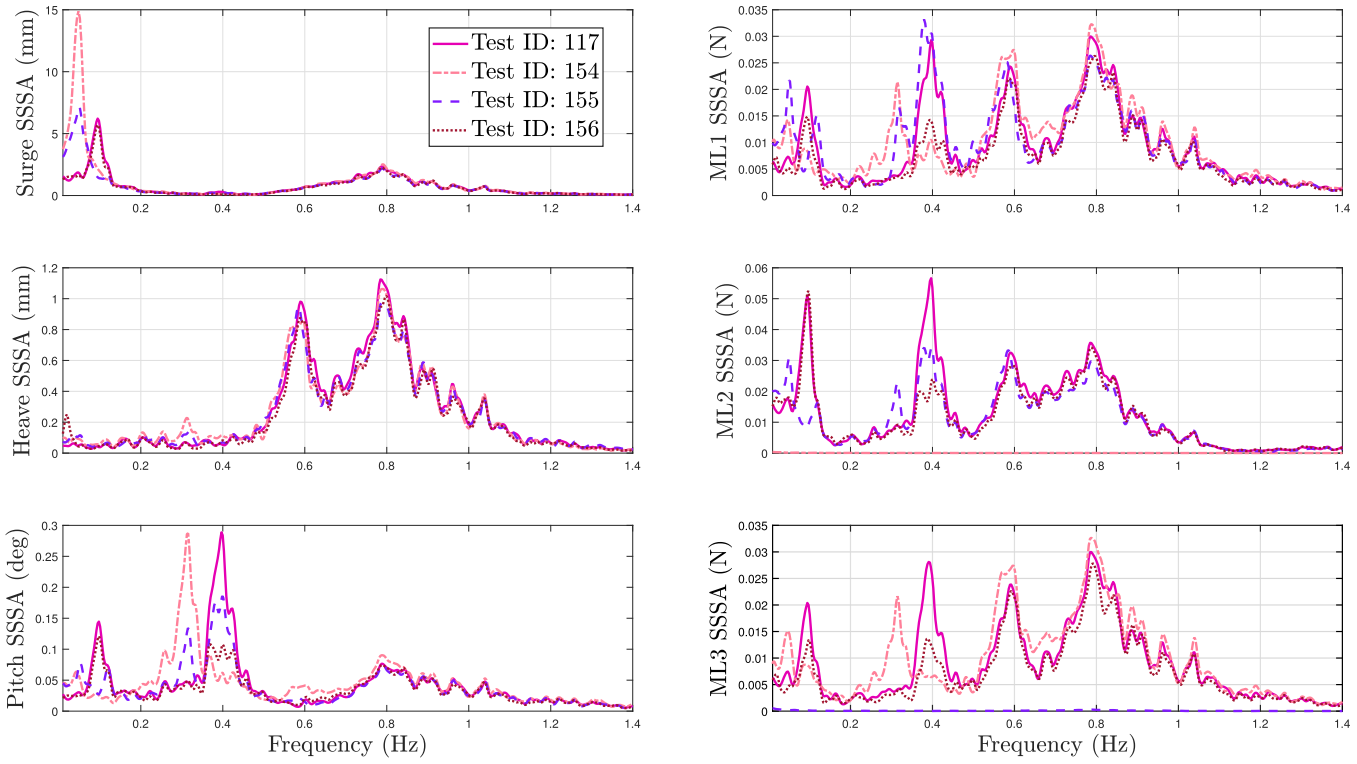


Fig. 25. Surge, heave, pitch and mooring lines frequency R response in different ALS conditions.

stiffness associated with heave and pitch is mainly governed by the inherent stiffness of the mooring lines, so variations in pre-tension do not impact their response as significantly.

The FFT analysis of the forward mooring line tension reveals prominent peaks at frequencies distinct from the peak period of the sea state. This indicates that tension in the mooring system is particularly sensitive to the resonant frequencies of surge, heave, and pitch. Minor variations in amplitude are observed at the low-frequency resonance points, highlighting a subtle influence of pre-tension on the response. However, the amplitude at the primary sea state frequency shows negligible variation, suggesting that pre-tension has minimal effect on tension response within this frequency band.

6.7. Accidental limit state test

To evaluate how the system responds under accidental damage conditions, ALS analyses were conducted on the moored structure under various damaged scenarios. The specific ALS tests performed are as follows:

- Test 154 simulates the disconnection of the forward mooring line.
- Test 155 simulates the disconnection of one of the two stern mooring lines.
- Test 156 simulates the failure of the actuators controlling the pitch angle of the turbine blades.

Fig. 25 presents the dynamic frequency responses associated with these specific tests for clearer analysis. Additionally, for comparison, the frequency response from a similar test with no damage (Test 117) is included. From the analysis of Fig. 25, the following conclusions can be drawn:

- In the wave frequency band, the dynamic response of the system remains relatively stable across all tests, indicating that the structural motions are not significantly affected.
- In the low-frequency band, however, significant changes in resonance periods and amplitudes are observed in the surge and pitch motions:
  - In Test 154, where the forward mooring line is disconnected, the pitch resonance frequency shifts closer to the resonance frequency of the structure in a free-floating state.
  - The surge resonance period also undergoes a substantial shift, causing the structure to oscillate at frequencies lower than those originally designed for.
  - In Test 156, where a thrust force acts on the turbine, no major differences are observed, apart from a decrease in the amplitude of pitch oscillation near the resonance frequency.

Fig. 26 shows the average values indicating the structural characteristics, providing further insights into the effects of damage on the system:

- In the reference test (Test 117), both surge and pitch average values are virtually zero, as the line pre-tension values are balanced and all mooring lines are intact.
- In Test 154, where the forward mooring line is absent, the pre-tension level in the remaining two lines is reduced, leading to a significant offset in both surge and pitch. This reduction in pre-tension, while preserving an unchanged frequency response, drastically lowers the probability of further mooring line failures.
- In Test 155, a similar effect is observed, but the offset is smaller in magnitude and occurs in the opposite direction compared to Test 154.
- Test 156 represents the most critical condition. Here, an increase of over 40 % in the average tension of the bowline is observed, along with substantial offset values. It is noteworthy that the thrust applied in this test was determined using numerical software (OrcaFlex) by locking the blades at a pitch angle of 0° and applying the rotor brake.

These analyses provide a comprehensive view of the dynamic of the system and average responses across different accidental damage con-

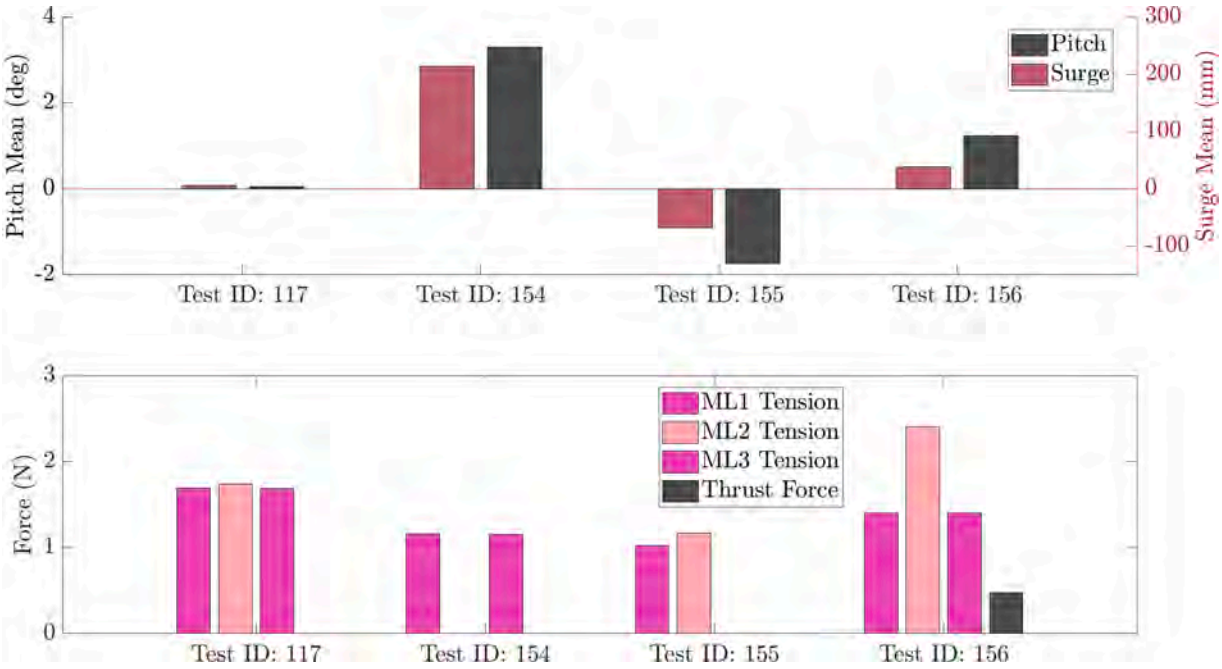


Fig. 26. Surge, pitch, mooring lines and thrust mean values in different ALS conditions.

ditions. The results help to assess the stability of the moored structure and highlight potential risks in both operational and failure scenarios.

7. Conclusions

In this paper, we have presented the dataset and findings from an extensive experimental campaign conducted at the Ship Hydromechanics Laboratory of Delft University of Technology, Faculty of Mechanical Engineering. The dataset, which includes all the tests described in this article, can be accessed at the following link. This repository provides freely downloadable CSV files containing the time histories of the tank tests, along with a readme file detailing the organization of the data. These resources are intended to facilitate validation of numerical models and to support further research within the scientific community. Detailed information about the mooring model and floating device is also provided to enable accurate calibration of these models.

The model setup and scaling procedure were carefully designed to ensure the results would be representative of the full-scale system. We began with a full-scale model featuring nylon mooring lines with constant axial stiffness. The model was then scaled down according to Froude scaling laws. For the scaled model, we replaced the nylon lines with springs, adjusting the stiffness to maintain a constant axial stiffness in accordance with Froude scaling. This approach allowed us to monitor the motions of the structure and the tensions in the mooring lines under controlled scaled laboratory conditions.

The goal of the experimental campaign was to evaluate the performance of a floating system moored with taut lines under operational, extreme (ULS), and damaged (ALS) conditions. A key focus of this study was the role of pre-tension in the mooring lines as an important factor influencing system behavior. To capture a wide range of realistic conditions, a series of wave and wind scenarios was designed based on an in-depth analysis of the site resources. This approach enabled a complete characterization of the system with a minimal number of tests, which included regular waves, irregular waves with wind, multisine waves for system identification, and extreme irregular waves with the turbine rotor parked.

A major finding of the campaign was that the dynamic response of the system, when moored with constant-stiffness lines (using springs), remained unaffected by the thrust force applied to the turbine. With mooring lines of constant stiffness, the thrust force primarily influences the mean tension in the mooring lines and the mean offset of the structure, as long as the lines do not experience slack. However, it should be noted that in this experimental model, wind turbulence is not replicated, which significantly impacts the low-frequency dynamics of the system, especially under operational conditions.

In the extreme irregular wave tests, which examined the resilience of the system under severe conditions, various levels of pre-tension were considered. While pre-tension had a limited effect on motion amplitudes and mean values in operational and irregular wave conditions, slight variations were observed in extreme waves (see Section 6.6). Higher pre-tension levels led to minor shifts in the resonance frequency of surge due to changes in geometrical stiffness (K_{11}). However, these shifts were not substantial enough to significantly impact the overall dynamic response of the system. The campaign also included tests simulating extreme events under damaged conditions, where the resilience of the system was assessed with a detached mooring line (ALS conditions). In these cases, the taut mooring configuration played a vital role in maintaining stability. When a line was detached, the loads on the remaining lines decreased due to the reduction of the system mooring stiffness, which led to increased motions. This reduction in stiffness also lowered the risk of cascading failures, effectively placing the system under “safe” conditions. With the loss of a mooring line, the motions of the floating structure increase considerably (see Figs. 26 and 25), making turbine operation unfeasible under damaged conditions.

This study highlights several advantages of taut mooring systems. These configurations provide excellent stability with minimal motion, which can improve turbine productivity and reduce fatigue loads on the structure. With such limited motion, the acceleration at the nacelle remains low, which is a critical parameter to consider for the fatigue life of the nacelle. Moreover, the shorter length and lower material requirements of taut mooring lines contribute to cost savings compared to semi-taut and catenary systems. However, the anchoring requirements for taut moorings present potential challenges, especially in complex seabed conditions. Further research is needed to address the installation complexities associated with anchoring in varying geological environments.

Future experimental campaigns could benefit from implementing a hardware-in-the-loop (HIL) system to simulate variable thrust. Such a system would adjust thrust dynamically based on the motion of the substructure and the ambient turbulence levels, providing a more realistic representation of operating conditions and further enhancing the accu-

racy of the obtained dynamic results. Future work will aim to replicate the nonlinear stiffness behavior of materials like nylon, whose rigidity depends on the load applied. Testing with nylon or polyester mooring lines that exhibit load-dependent stiffness will be particularly interesting, as it would bring the study closer to practical, real-world conditions.

Declaration of competing interest

The authors declare the following financial interests/personal relationships which may be considered as potential competing interests:

Francesco Niosi reports financial support was provided by Polytechnic of Turin Department of Mechanical and Aerospace Engineering. If there are other authors, they declare that they have no known competing financial interests or personal relationships that could have appeared to influence the work reported in this paper.

CRediT authorship contribution statement

Francesco Niosi: Writing – review & editing, Writing – original draft, Validation, Software, Methodology, Investigation, Formal analysis, Data curation, Conceptualization; **Oronzo Dell'edera:** Writing – original draft, Validation, Software, Methodology, Investigation, Formal analysis, Data curation, Conceptualization; **Mattia Glorioso:** Software, Investigation, Data curation; **Bruno Paduano:** Writing – original draft, Supervision, Methodology, Investigation; **Giuseppe Giorgi:** Supervision, Methodology, Funding acquisition; **Sebastian Schreier:** Supervision, Project administration, Investigation, Funding acquisition, Data curation

Appendix A.

Table 16.

Table 16
List of abbreviations.

Abbreviations	Meanings
AETFE	Averaged Experimental Transfer Function Estimate
ALS	Accidental Limit State
CDF	Cumulative Distribution Function
CETA	Clean Energy Transition Agenda
CFD	Computational Fluid Dynamics
CoG	Center of Gravity
DNV	Det Norske Veritas
DoF	Degree of Freedom
EC	Environmental Contour
ECMWF	European Centre for Medium-Range Weather Forecasts
ERA5	fifth generation ECMWF atmospheric reanalysis
FFT	Fast Fourier Transform
FOWT	Floating Offshore Wind Turbine
GEV	Generalized Extreme Value
H_s	Significant Wave Height
ITTC	International Towing Tank Conference
LC	Load Cell
LCS_i	Layout Configuration Spring with i pre-tension
ML	Mooring Line
MOSS	Maximum Operative Sea State
NREL	National Renewable Energy Laboratory
PDF	Probability Density Function
POT	Peak Over Threshold
RAO	Response Amplitude Operator
SSSA	Single Side Spectrum Amplitude
SWL	Sea Water Level
T_p	Peak Period
ULS	Ultimate Limit State
WG	Wave Gauge
W_s	Wind Speed

Table 17
Environmental contour parameters.

	Parameter name	Value fitted
Weibull distribution for H_s	γ	0.400
	λ	0.794
	κ	1.104
Parameters of $\mu(x)$	a_0	0.444
	a_1	1.272
	a_2	0.227
	R^2_{adj}	0.9997
Parameters of $\sigma(x)$	b_0	0.0435
	b_1	0.239
	b_2	0.498
	R^2_{adj}	0.9921
Parameters of $\kappa(x)$	c_0	4.56
	c_1	0.0284
	c_2	3.58
	R^2_{adj}	0.9569
Parameters of $\lambda(x)$	d_0	−3.07
	d_1	11.3
	d_2	0.48
	R^2_{adj}	0.9999
Parameters of $\lambda(w)$	e_0	0.9577
	e_1	0.0036
	e_2	2.223
	R^2_{adj}	0.9982
Parameters of $\kappa(w)$	f_0	1.69
	f_1	2.68e−5
	f_2	3.815
	R^2_{adj}	0.9757

Table 18
Empty tank tests, regular waves: wave height results.

		Wave heigth [mm]						Wave heigth variation %				
ID	Wave name	Target	WG1	WG2	WG3	WG4	WG5	WG1	WG2	WG3	WG4	WG5
004	*RW_ND_OP_*01	11.7	11.6	11.7	11.1	12.2	11.4	0.7%	−0.1%	5.1%	−3.9%	2.2%
006	*RW_ND_OP_*02	15.9	13.9	15.7	13.4	14.9	14.1	12%	1.5%	16%	6.3%	12%
007	*RW_ND_OP_*03	20.8	21.5	22.1	20.3	21.8	21.1	−3.1%	−6.4%	2.6%	−4.8%	−1.3%
009	*RW_ND_OP_*04	26.3	25.8	25.1	27.1	25.7	28.0	1.8%	4.6%	−2.9%	2.4%	−6.5%
010	*RW_ND_OP_*05	32.5	34.9	33.3	34.4	33.2	34.5	−7.3%	−2.4%	−6.0%	−2.1%	−6.3%
023	*RW_ND_OP_*06	46.8	47.7	41.6	45.0	46.9	47.2	−1.9%	11%	3.9%	−0.2%	−0.9%
015	*RW_ND_OP_*07	17.6	18.3	18.9	17.2	18.6	18.4	−4.0%	−7.7%	2.1%	−6.0%	−5.0%
016	*RW_ND_OP_*08	31.2	30.8	32.9	29.2	31.2	31.2	1.3%	−5.5%	6.3%	−0.1%	−0.1%
024	*RW_ND_OP_*09	70.2	70.2	70.0	71.5	75.8	74.2	−0.1%	0.3%	−1.9%	−8.0%	−5.7%
018	*RW_ND_OP_*10	29.3	31.3	26.1	29.4	28.0	25.8	−7.2%	11%	−0.5%	4.3%	12%
020	*RW_ND_OP_*11	52.0	54.2	52.3	56.9	56.5	57.7	−4.3%	−0.5%	−9.4%	−8.6%	−11%
021	*RW_ND_OP_*12	117	120	135	133	133	133	−2.8%	−15%	−13%	−14%	−14%

Table 19
Empty tank tests, irregular waves: significant wave height results.

		Wave heigth [mm]						Wave heigth delta %				
ID	Wave name	Target	WG1	WG2	WG3	WG4	WG5	WG1	WG2	WG3	WG4	WG5
047	*IW_ND_OP_*01	13.4	12.5	12.8	12.5	12.7	11.9	−7.3%	−4.5%	−7.0%	−5.5%	−11%
029	*IW_ND_OP_*02	14.3	12.4	12.9	12.5	12.6	13.0	−13%	−9.6%	−12%	−12%	−8.9%
049	*IW_ND_OP_*03	15.6	14.9	15.0	14.6	14.7	14.2	−4.6%	−4.0%	−6.6%	−5.9%	−9.1%
050	*IW_ND_OP_*04	17.4	16.7	17.6	16.6	16.6	16.7	−4.0%	1.2%	−4.6%	−4.6%	−4.0%
036	*IW_ND_OP_*05	19.9	18.8	18.1	19.3	18.3	19.1	−5.5%	−9.0%	−3.0%	−8.0%	−4.0%
037	*IW_ND_OP_*06	22.9	20.9	22.3	21.8	22.7	21.7	−8.8%	−2.7%	−4.9%	−0.9%	−5.3%
038	*IW_ND_OP_*07	26.7	27.0	27.0	27.2	26.9	26.0	1.3%	1.3%	2.0%	0.9%	−2.5%
039	*IW_ND_OP_*08	31.3	31.4	32.4	30.6	31.9	30.4	0.5%	3.7%	−2.1%	2.1%	−2.7%
051	*IW_ND_OP_*09	36.7	36.5	38.0	35.0	37.0	35.0	−0.5%	3.6%	−4.5%	0.9%	−4.5%
041	*IW_ND_OP_*10	43.0	43.4	43.5	42.4	44.0	44.8	0.9%	1.1%	−1.4%	2.3%	4.1%
042	*IW_ND_OP_*11	50.3	51.9	53.0	53.5	51.8	52.9	3.2%	5.3%	6.3%	3.0%	5.1%
043	*IW_ND_OP_*12	58.5	58.7	61.0	61.4	61.9	61.8	0.3%	4.2%	4.9%	5.7%	5.6%
044	*IW_ND_EX_s*01	86.1	84.0	88.9	88.0	88.9	87.4	−2.5%	3.2%	2.2%	3.2%	1.5%
045	*IW_ND_EX_s*02	86.1	86.2	93.3	90.0	89.6	89.3	0.1%	8.3%	4.5%	4.0%	3.7%
046	*IW_ND_EX_s*03	86.1	86.3	91.0	86.7	89.4	88.4	0.2%	5.6%	0.6%	3.8%	2.6%

Table 20
Empty tank tests, irregular waves: energetic period (Te) results.

		Energetic period Te [s]						Energetic period Te delta %				
ID	Wave name	Target	WG1	WG2	WG3	WG4	WG5	WG1	WG2	WG3	WG4	WG5
047	*IW_ND_OP_*01	0.57	0.60	0.61	0.61	0.60	0.61	6.2%	8.0%	8.0%	6.2%	8.0%
029	*IW_ND_OP_*02	0.57	0.63	0.63	0.64	0.60	0.62	9.7%	9.7%	11%	4.5%	8.0%
049	*IW_ND_OP_*03	0.59	0.63	0.63	0.64	0.63	0.63	6.8%	6.8%	8.5%	6.8%	6.8%
050	*IW_ND_OP_*04	0.61	0.65	0.64	0.65	0.65	0.65	6.5%	4.8%	6.5%	6.5%	6.5%
036	*IW_ND_OP_*05	0.64	0.69	0.69	0.69	0.69	0.69	8.4%	8.4%	8.4%	8.4%	8.4%
037	*IW_ND_OP_*06	0.67	0.88	0.75	0.75	0.74	0.74	32%	12%	12%	11%	11%
038	*IW_ND_OP_*07	0.70	0.76	0.75	0.75	0.75	0.75	8.2%	6.8%	6.8%	6.8%	6.8%
039	*IW_ND_OP_*08	0.74	0.79	0.79	0.79	0.78	0.79	6.3%	6.3%	6.3%	5.0%	6.3%
051	*IW_ND_OP_*09	0.79	0.81	0.83	0.82	0.83	0.83	2.7%	5.2%	4.0%	5.2%	5.2%
041	*IW_ND_OP_*10	0.84	0.88	0.88	0.88	0.87	0.88	4.9%	4.9%	4.9%	3.7%	4.9%
042	*IW_ND_OP_*11	0.89	0.94	0.94	0.94	0.93	0.94	5.3%	5.3%	5.3%	4.2%	5.3%
043	*IW_ND_OP_*12	0.95	0.98	0.99	0.99	0.99	0.99	3.1%	4.2%	4.2%	4.2%	4.2%
044	*IW_ND_EX_s*01	1.13	1.16	1.16	1.16	1.16	1.16	2.9%	2.9%	2.9%	2.9%	2.9%
045	*IW_ND_EX_s*02	1.13	1.15	1.16	1.16	1.14	1.15	2.0%	2.9%	2.9%	1.1%	2.0%
046	*IW_ND_EX_s*03	1.13	1.18	1.18	1.18	1.17	1.17	4.7%	4.7%	4.7%	3.8%	3.8%

Table 21
Free decay tests.

Test ID	Test name	Pre-tension ID
057	*FD_Moor_Surge*	LCS1
061	*PL_Moor_Sway*	LCS1
065	*FD_Moor_Heave*	LCS1
066	*FD_Moor_Roll*	LCS1
069	*FD_Moor_Pitch*	LCS1
074	*FD_Moor_Yaw*	LCS1
163	*FD_NoMoor_Heave*	\
168	*FD_NoMoor_Pitch*	\
171	*FD_NoMoor_Roll*	\

Table 22
Regular waves tests with design pre-tension value (LCS1).

Test ID	Test name	Empty tank wave ID	Pre-tension ID
083	*RW_NW_OP*_01	004	LCS1
084	*RW_NW_OP*_02	006	LCS1
085	*RW_NW_OP*_03	007	LCS1
086	*RW_NW_OP*_04	009	LCS1
087	*RW_NW_OP*_05	010	LCS1
088	*RW_NW_OP*_06	023	LCS1
089	*RW_NW_OP*_07	015	LCS1
090	*RW_NW_OP*_08	016	LCS1
091	*RW_NW_OP*_09	024	LCS1
092	*RW_NW_OP*_10	018	LCS1
093	*RW_NW_OP*_11	020	LCS1
094	*RW_NW_OP*_12	021	LCS1

Table 23
Operative irregular waves tests with design pre-tension value (LCS1).

Test ID	Test name	Empty tank wave ID	Pre-tension ID
095	*IW_OP*_01	047	LCS1
096	*IW_OP*_02	029	LCS1
097	*IW_OP*_03	049	LCS1
098	*IW_OP*_04	050	LCS1
100	*IW_OP*_06	037	LCS1
101	*IW_OP*_07	038	LCS1
102	*IW_OP*_08	039	LCS1
103	*IW_OP*_09	051	LCS1
104	*IW_OP*_10	041	LCS1
105	*IW_OP*_11	042	LCS1
106	*IW_OP*_12	043	LCS1
113	*IW_OP*_05_*s*02	\	LCS1
114	*IW_OP*_05_*s*03	\	LCS1
115	*IW_OP*_05_*s*04	\	LCS1
116	*IW_OP*_05_*s*05	\	LCS1
128	*IW_OP*_05	036	LCS1
129	*IW_OP*_05	036	LCS1
130	*IW_OP*_05	036	LCS1
131	*IW_OP*_05	036	LCS1
132	*IW_OP*_05	036	LCS1
133	*IW_OP*_05	036	LCS1
134	*IW_OP*_05	036	LCS1
135	*IW_OP*_05	036	LCS1
136	*IW_OP*_05	036	LCS1

Table 24
Extreme irregular waves tests with design pre-tension value (LCS1).

Test ID	Test name	Empty tank wave ID	Pre-tension ID
107	*IW_EX_PR_s*01	044	LCS1
110	*IW_EX_PR_s*02	045	LCS1
112	*IW_EX_PR_s*03	046	LCS1
117	*IW_EX_PR_s*04	\	LCS1
118	*IW_EX_PR_s*05	\	LCS1

Table 25
System ID waves tests with design pre-tension value (LCS1).

Test ID	Test name	Empty tank wave ID	Pre-tension ID
119	*MS_CA_Stmax*_28	210	LCS1
120	*MS_CA_Stmax*_19	211	LCS1
121	*MS_CA_Stmax*_14	212	LCS1
123	*MS_CA_Stmax*_11	213	LCS1
124	*MS_CA_Stmax*_9	214	LCS1

Table 26
Irregular and system ID waves tests with off-design pre-tension values.

Test ID	Test name	Empty tank wave ID	Pre-tension ID
144	*IW_OP*_05	036	LCS2
145	*MS_CA_Stmax*_19	211	LCS2
146	*MS_CA_Stmax*_11	212	LCS2
147	*IW_EX_PR_s*04	\	LCS2
149	*IW_OP*_05	036	LCS3
150	*MS_CA_Stmax*_19	211	LCS3
151	*MS_CA_Stmax*_11	212	LCS3
152	*IW_EX_PR_s*04	\	LCS3
157	*IW_OP*_05	036	LCS4
159	*MS_CA_Stmax*_11	212	LCS4
160	*IW_EX_PR_s*04	\	LCS4
162	*MS_CA_Stmax*_19	211	LCS4
196	*MS_CA_Stmax*_19	211	LCS5
197	*MS_CA_Stmax*_11	212	LCS5
198	*IW_EX_PR_s*04	\	LCS5
199	*IW_OP*_05	036	LCS5

Table 27
ALS tests.

Test ID	Test name	Empty tank wave ID	Pre-tension ID
154	*ALS_EX_PR_s*04	\	LCS1 damaged 1
155	*ALS_EX_PR_s*04	\	LCS1 damaged 2
156	*ALS_EX_s*04	\	LCS1 damaged 3

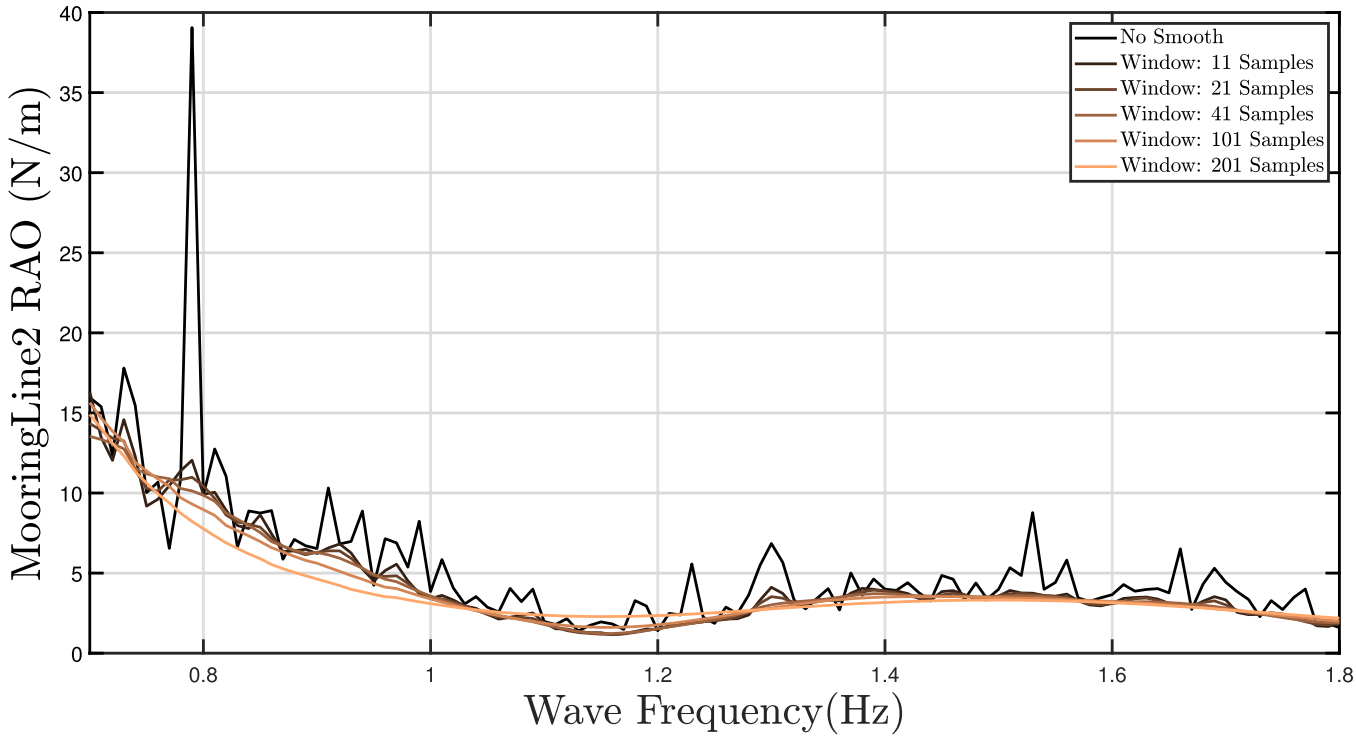


Fig. 27. AETFE sensitivity analysis: variation on number of samples for smoothing.

References

Azcona, J., Bouchotrouch, F., González, M., Garciandía, J., Munduate, X., Kelberlau, F., Nygaard, T.A., 2014. Aerodynamic thrust modelling in wave tank tests of offshore floating wind turbines using a ducted fan. Vol. 524. https://doi.org/10.1088/1742-6596/524/1/012089

Bach-Gansmo, M.T., Garvik, S.K., Thomsen, J.B., Andersen, M.T., 2020. Parametric study of a taut compliant mooring system for a FOWT compared to a catenary mooring. J. Mar. Sci. Eng. 8 (6), 431. https://doi.org/10.3390/jmse8060431

Barltrop, N., 1998. Floating structures: a guide for design and analysis.

Chen, C., Ma, Y., Fan, T., 2022. Review of model experimental methods focusing on aerodynamic simulation of floating offshore wind turbines. Renew. Sustain. Energy Rev. 157, 112036. https://doi.org/10.1016/j.rser.2021.112036

Deb, K., Pratap, A., Agarwal, S., Meyarivan, T., 2002. A fast and elitist multiobjective genetic algorithm: NSGA-II. IEEE Trans. Evol. Comput. 6 (2), 182–197. https://doi.org/10.1109/4235.996017

DNVGL-RP-C205, 2017. Environmental conditions and environmental loads.

Fontana, M., Casalone, P., Sirigu, S.A., Giorgi, G., Bracco, G., Mattiazzo, G., 2020. Viscous damping identification for a wave energy converter using CFD-URANS simulations. J. Mar. Sci. Eng. 8 (5), 355. https://doi.org/10.3390/jmse8050355

Ghigo, A., Niosi, F., Paduano, B., Bracco, G., Mattiazzo, G., 2022. Mooring System Design and Analysis for a Floating Offshore Wind Turbine in Pantelleria Volume 11: Wind Energy. https://doi.org/10.1115/GT2022-83219

Hallak, T.S., Guedes Soares, C., Sainz, O., Hernández, S., Arévalo, A., 2022. Hydrodynamic analysis of the WIND-bos spar floating offshore wind turbine. J. Mar. Sci. Eng. 10 (12). https://doi.org/10.3390/jmse10121824

Hasselmann, K., Barnett, T.P., Bouws, E., Carlson, H., Cartwright, D.E., Enke, K., Ewing, J.A., Gienapp, H., Hasselmann, D.E., Kruseman, P., Meerburg, A., Muller, P., Olbers, D.J., Richter, K., Sell, W., Walden, H., 1973. Measurements of wind-wave growth and swell decay during the joint north sea wave project (JONSWAP). Deut. Hydrogr. Z. 8 (1), 1–95.

Hersbach, H., Bell, B., Berrisford, P., Hirahara, S., Horányi, A., Muñoz-Sabater, J., Nicolas, J., Peubey, C., Radu, R., Schepers, D., 2020. The ERA5 global reanalysis. Q. J. R. Meteorolog. Soc. 146 (730), 1999–2049. https://doi.org/10.1002/qj.3803

ITTC, H., 2014. Guide to the expression of uncertainty in experimental hydrodynamics.

Jonkman, J., Butterfield, S., Musial, W., Scott, G., 2009. Definition of a 5-MW reference wind turbine for offshore system development https://doi.org/10.2172/947422

Jonkman, J.M., 2010. Definition of the floating system for phase IV of OC3. https://doi.org/10.2172/979456

Kimball, R.W., Sclavounos, P.D., Cross, G.M., 2005. Hydrodynamic considerations in the design of floating wind turbine support structures. In: Proceedings of the 24th International Conference on Offshore Mechanics and Arctic Engineering. ASME.

Kimpián, T., Augusztinovicz, F., 2016. Multiphase multisine signals–theory and practice. In: Proceedings of ISMA2016 including USD2016, International Conference on Noise and Vibration Engineering, pp. 19–21. https://past.isma-isaac.be/downloads/isma2016/papers/isma2016_0570.pdf.

Lopez-Olocco, T., Liang, G., Medina-Manuel, A., Ynocente, L.S., Jiang, Z., Souto-Iglesias, A., 2023. Experimental comparison of a dual-spar floating wind farm with shared mooring against a single floating wind turbine under wave conditions. Eng. Struct. 292. https://doi.org/10.1016/j.engstruct.2023.116475

Martin, H.R., 2011. Development of a scale model wind turbine for testing of offshore floating wind turbine systems. https://api.semanticscholar.org/CorpusID:107858426.

Martínez-Estévez, I., Domínguez, J.M., Tagliafierro, B., Canelas, R.B., García-Feal, O., Crespo, A.J.C., Gómez-Gesteira, M., 2023. Coupling of an SPH-based solver with a multiphysics library. Comput. Phys. Commun. 283, 108581. https://doi.org/10.1016/j.cpc.2022.108581

Metsch, Y., 2023. Experimental low frequency mooring analysis of a floating offshore wind turbine. Ms thesis. Delft University of Technology. Delft, NL. http://resolver.tudelft.nl/uuid:1affcb99-6d22-4630-a1de-fc8a13e706c7.

MORE, Marine offshore renewable energy lab. Available online: http://www.morenergylab.polito.it/, Accessed on September 15th, 2023.

Moscoloni, C., Zarra, F., Novo, R., Giglio, E., Vargiu, A., Mutani, G., Bracco, G., Mattiazzo, G., 2022. Wind turbines and rooftop photovoltaic technical potential assessment: application to Sicilian minor islands. Energies 15 (15), 5548. https://doi.org/10.3390/en15155548

Myhr, A., Maus, K.J., Nygaard, T.A., 2011. Experimental and computational comparisons of the OC3-HYWIND and tension-leg-buoy (TLB) floating wind turbine conceptual designs. pp. ISOPE–I–11–560.

Myhr, A., Nygaard, T.A., 2015. Comparison of experimental results and computations for tension-leg-buoy offshore wind turbines.

NaturalPoint, Motion capture systems – optitrack webpage. Available online: https://www.optitrack.com/, Accessed on September 15th, 2023.

Niosi, F., Begovic, E., Bertorello, C., Rinauro, B., Sannino, G., Bonfanti, M., Sirigu, S.A., 2023a. Experimental validation of orcaflex-based numerical models for the PEWEC device. Ocean Eng. 281, 114963. https://doi.org/10.1016/j.oceaneng.2023.114963

Niosi, F., Dell'Edera, O., Schreier, S., 2023b. Experimental dataset of taut-leg mooring system for FOWT. https://doi.org/10.4121/9f32fe66-ec63-4cad-bf6a-7e9fe62d68e8.v1

Niosi, F., Dell'Edera, O., Sirigu, M., Ghigo, A., Bracco, G., 2023c. A comparison between different numerical models and experimental tests for the study of floating offshore wind turbines. In: The 33rd International Ocean and Polar Engineering Conference.

Paduano, B., Parrinello, L., Niosi, F., Dell'Edera, O., Sirigu, S.A., Faedo, N., Mattiazzo, G., 2024. Towards standardised design of wave energy converters: a high-fidelity modelling approach. Renew. Energy 224, 120141. https://doi.org/10.1016/j.renene.2024.120141

PNRR isole verdi. Available online: www.mase.gov.it/pagina/pnrr-isole-verdi.

Robertson, A., Jonkman, J., Masciola, M., Song, H., Goupee, A., Coulling, A., Luan, C., 2014. Definition of the semisubmersible floating system for phase II of OC4. Technical Report. National Renewable Energy Lab.(NREL), Golden, CO (United States). https://doi.org/10.2172/1155123

Robertson, A.N., Gueydon, S., Bachynski, E., Wang, L., Jonkman, J., Alarcón, D., Amet, E., Beardsell, A., Bonnet, P., Boudet, B., Brun, C., Chen, Z., Féron, M., Forbush, D., Galinos, C., Galvan, J., Gilbert, P., Gómez, J., Harnois, V., Haudin, F., Hu, Z., Le Dreff,

J., Leimeister, M., Lemmer, F., Li, H., Mckinnon, G., Mendikoa, I., Moghtadaei, A., Netzband, S., Oh, S., Pegalajar-Jurado, A., Nguyen, M.Q., Ruehl, K., Schünemann, P., Shi, W., Shin, H., Si, Y., Surmont, F., Trubat, P., Qwist, J., Wohlfahrt-Laymann, S., 2020. OC6 phase I: investigating the underprediction of low-frequency hydrodynamic loads and responses of a floating wind turbine. J. Phys. 1618 (3), 032033. https://doi.org/10.1088/1742-6596/1618/3/032033

Robertson, A.N., Jonkman, J.M., 2011. Loads analysis of several offshore floating wind turbine concepts. In: Proceedings of the International Offshore and Polar Engineering Conference. NREL/CP-5000-50135.

Robertson, A.N., Wendt, F., Jonkman, J.M., Popko, W., Dagher, H., Gueydon, S., Qvist, J., Vittori, F., Azcona, J., Uzunoglu, E., Soares, C.G., Harries, R., Yde, A., Galinos, C., Hermans, K., de Vaal, J.B., Bozonnet, P., Bouy, L., Bayati, I., Bergua, R., Galvan, J., Mendikoa, I., Sanchez, C.B., Shin, H., Oh, S., Molins, C., Debruyne, Y., 2017. OC5 project phase II: validation of global loads of the deepcwind floating semisubmersible wind turbine. Energy Procedia 137, 38–57. 14th Deep Sea Offshore Wind RnD Conference, EERA DeepWind'2017. https://doi.org/10.1016/j.egypro.2017.10.333

Robertson, A.N., Wendt, F.F., Jonkman, J.M., Popko, W., Vorpahl, F., Stansberg, C.T., Bachynski, E.E., Bayati, I., Beyer, F., de Vaal, J.B., et al., 2015. Oc5 project phase I: Validation of hydrodynamic loading on a fixed cylinder. In: ISOPE International Ocean and Polar Engineering Conference. ISOPE, pp. ISOPE–I.

Roddier, D., Cermelli, C.A., Aubault, A., Weinstein, A., 2010. Windfloat: a floating foundation for offshore wind turbines. J. Renew. Sustain. Energy 2, 033104. https://doi.org/10.1063/1.3435339

Seaflex. Available online: www.seaflex.com/products/seaflex-spring/, Accessed on October 18th, 2023.

Secretariat, C., Clean Energy Transition Agenda (CETA). Available online: https://clean-energy-islands.ec.europa.eu/assistance/clean-energy-transition-agenda, Accessed on September 15th 2023.

Stewart, G., Muskulus, M., 2016. A review and comparison of floating offshore wind turbine model experiments. Energy Procedia 94, 227–231. 13th Deep Sea Offshore Wind RnD Conference, EERA DeepWind'2016. https://doi.org/10.1016/j.egypro.2016.09.228

Sørum, S.H., Fonseca, N., Kent, M., Faria, R.P., 2023. Modelling of synthetic fibre rope mooring for floating offshore wind turbines. J. Mar. Sci. Eng. 11 (1), 193. https://doi.org/10.3390/jmse11010193

Tagliafierro, B., Karimirad, M., Altomare, C., Göteman, M., Martínez-Estévez, I., Capasso, S., Domínguez, J.M., Viccione, G., Gómez-Gesteira, M., Crespo, A. J.C., 2023. Numerical validations and investigation of a semi-submersible floating offshore wind turbine platform interacting with ocean waves using an SPH framework. Appl. Ocean Res. 141, 103757. https://doi.org/10.1016/j.apor.2023.103757

The European Commission. The European Green Deal. Technical Report. Available online: https://commission.europa.eu/strategy-and-policy/priorities-2019-2024/european-green-deal_en, Accessed on September 15th 2023.

The Syrope Method for Stiffness Testing of Polyester Ropes, Volume 1: Offshore Technology. (2018). https://asmedigitalcollection.asme.org/OMAE/proceedings-pdf/OMAE2018/51203/V001T01A067/2534818/v001t01a067-omae2018-77944.pdf. https://doi.org/10.1115/OMAE2018-77944

Thiagarajan, K.P., Troesch, A.W., 1994. Modeling of ocean structures: scale effects and scaling issues. J. Offshore Mech. Arct. Eng. 116, 289–295.

Utsunomiya, T., Sato, T., Matsukuma, H., Yago, K., 2009. Experimental validation for motion of a SPAR-type floating offshore wind turbine using 1/22.5 scale model. pp. 951–959. https://doi.org/10.1115/OMAE2009-79695

Veritas, D.N., Lloyd, G., 2017. Recommended practice for design, testing and analysis of offshore fibre ropes (DNVGL-RP-e305).

Vigara, F., Cerdán, L., Durán, R., Muñoz, S., Lynch, M., Doole, S., Molins, C., Trubat, P., Guanche, R., 2019. D1.2 Design Basis. Technical Report. COREWIND Consortium. https://corewind.eu/wp-content/uploads/files/publications/COREWIND-D1.2-03-Design-Basis.pdf.

Update

Ocean Engineering

Volume 329, Issue , 15 June 2025, Page

DOI: https://doi.org/10.1016/j.oceaneng.2025.121214

Ocean Engineering 329 (2025) 121214



Contents lists available at ScienceDirect

Ocean Engineering

journal homepage: www.elsevier.com/locate/oceaneng





"Experimental investigation and dataset release of a taut-leg mooring system for a semi-submersible floating offshore wind turbine" [Ocean Eng. 328 1 (2025) 121067

Niosi Francesco [a,*], Dell'edera Oronzo [a], Glorioso Mattia [a], Paduano Bruno [a], Giorgi Giuseppe [a], Schreier Sebastian [b]

[a] *Marine Offshore Renewable Energy Lab (MOREnergy Lab), Department of Mechanical and Aerospace Engineering (DIMEAS), Politecnico di Torino, Via Duca Degli Abbruzzi, 24, Turin, 10129, Italy*

[b] *Delft University of Technology, Fac. Mechanical Engineering, Dept. Maritime Transport Technology, Ship Hydromechanics, Mekelweg 2, Delft, 2628 CD, Netherlands*

The authors regret an omission in the Acknowledgments and would like to revise it as follows:

Project funded under the National Recovery and Resilience Plan (NRRP), Italy, Mission 4 Component 2 Investment 1.3 - Call for tender No. 1561 of 11.10.2022 of Ministero dell' Universitá e della Ricerca (MUR); funded by the European Union – NextGenerationEU Award Number: Project code PE0000021, Concession Decree No. 1561 of 11.10.2022 adopted by Ministero dell'Universitá e della Ricerca (MUR), Italy, CUP, Italy E13C22001890001, Project title "Network 4 Energy Sustainable Transition – NEST".

The authors would like to apologise for any inconvenience caused.

DOI of original article: https://doi.org/10.1016/j.oceaneng.2025.121067.

* Corresponding author.
E-mail address: francesco.niosi@polito.it (N. Francesco).

https://doi.org/10.1016/j.oceaneng.2025.121214

Available online 15 April 2025

0029-8018/© 2025 The Author(s). Published by Elsevier Ltd. This is an open access article under the CC BY license (http://creativecommons.org/licenses/by/4.0/).